1 **Title** 2 Image3C, a multimodal image-based and label independent integrative method for single-cell 3 analysis 4 5 **Authors** Alice Accorsi^{1,†}, Andrew C. Box^{1,†}, Robert Peuß^{1,2,†}, Christopher Wood¹, Alejandro Sánchez 6 Alvarado^{1,3,#},*, Nicolas Rohner^{1,4,#} 7 [†]These authors contributed equally to this study 8 *These authors share senior authorship 9 10 *Author for correspondence: Alejandro Sánchez Alvarado (asa@stowers.org) 11 12 **Affiliation** 13 ¹Stowers Institute for Medical Research, Kansas City, MO, United States ²Institute for Evolution and Biodiversity, University of Münster, Münster, Germany 14 15 ³Howard Hughes Medical Institute, Stowers Institute for Medical Research, Kansas City, MO, 16 **United States** 17 ⁴Department of Molecular and Integrative Physiology, KU Medical Center, Kansas City, KS, 18 **United States** 19 20 **Running headline** 21 Image3C, tool for *de novo* morphology-based cell clustering

22

23

Abstract

Image-based cell classification has become a common tool to identify phenotypic changes in cell populations. However, this methodology is limited to organisms possessing well characterized species-specific reagents (e.g., antibodies) that allow cell identification, clustering and convolutional neural network (CNN) training. In the absence of such reagents, the power of image-based classification has remained mostly off-limits to many research organisms. We have developed an image-based classification methodology we named Image3C (Image-Cytometry Cell Classification) that does not require species-specific reagents nor pre-existing knowledge about the sample. Image3C combines image-based flow cytometry with an unbiased, high-throughput cell cluster pipeline and CNN integration. Image3C exploits intrinsic cellular features and non-species-specific dyes to perform *de novo* cell composition analysis and to detect changes in cellular composition between different conditions. Therefore, Image3C expands the use of imaged-based analyses of cell population composition to research organisms in which detailed cellular phenotypes are unknown or for which species-specific reagents are not available.

Impact statement

Image3C analyzes cell population composition through image-based clustering and neural network training, in research organisms devoid of species-specific reagents or pre-existing knowledge on cell phenotypes.

Introduction

46

47

48

49

50

51

52

53

54

55

56

57

58

59

60

61

62

63

64

65

66

67

68

Single-cell analysis have proven crucial to our understanding of fundamental biological processes such as development, homeostasis, regeneration, aging and disease (Goolam et al., 2016; Kimmel et al., 2019; Pepe-Mooney et al., 2019; Philippeos et al., 2018; Tirosh et al., 2016). High-throughput analyses of these and other biological processes at single cell-resolution require technologies capable of describing individual cells and subsequently clustering them based on similarities of features like morphology, cell surface protein expression or transcriptome profile. Recent advances in image-based cell profiling and single-cell RNA sequencing (scRNA-seq) allow quantification of differences between cell populations and comparisons of cell type composition between samples (Caicedo et al., 2017). Single-cell studies that use traditional research organisms (e.g., mouse, rat or fruit fly) benefit from the availability of genomic platforms and established antibody libraries. However, the same cannot be said for a growing number of important, yet understudied research organism lacking such reagents and whose biological interrogation would benefit immensely from single-cell analyses. In these cases, classical histochemical methods are often used to identify and characterize specific cells. Yet, the successful identification and enumeration of biologically meaningful cell types in such studies can be harmed by both the limited number and variety of cellular attributes (few features or low dynamic range) available for determination of cell types, and by observer bias when using traditional, hand-counting approaches (e.g., hemocytometer and Giemsa stain) (van der Meer, Scott, & de Keijzer, 2004). These shortcomings, together with the lack of extensive knowledge on cell-specific phenotypes available for training or for a priori assumptions usually results in the underestimation of the complexity of cellular composition or interactions among cell types within tissues.

Automated classification of cells using convolutional neural networks (CNN, machine learning method specialized in image recognition and classification) has become a promising approach for accurate high-throughput cell analysis that is free from observer bias (Blasi et al., 2016; Eulenberg et al., 2017; Kobayashi et al., 2017; Lei et al., 2018; Nassar et al., 2019; Suzuki et al., 2019). To date, CNN-based automated clustering and classification techniques require preexisting knowledge about the organism or cell type of interest (e.g., cell specific morphological traits within an image set) or the availability of cell-specific reagents (e.g., antibodies), or genomic sequence (e.g., single-cell sequencing) (Table 1 shows an overview of the existing methods) (Baron et al., 2019; Blasi et al., 2016; Cheng et al., 2021; Eulenberg et al., 2017; Hennig et al., 2017; Kobayashi et al., 2017; Lei et al., 2018; Nassar et al., 2019). This means that to make effective use of artificial intelligence (AI) approaches for single-cell analysis, one must have information available to train the algorithm or for machine learning (ML) models, which often arises in the form of information gleaned from the use of reagents like antibodies. Research areas that rely on inter-species comparisons or studies on emerging research organisms would benefit from single cell-based analyses that do not require pre-existing knowledge of cell types (i.e., which is required for training a CNN for example) and/or availability of antibodies or molecular databases. For example, within the interdisciplinary field of eco-immunology, a growing number of researchers is investigating immune system adaptation to different environments by studying immune cell compositions in diverse animals (Maizels & Nussey, 2013). Given the influences of immune cell composition on the immune system response of an organism (Kaczorowski et al., 2017), applying modern single cell analysis in eco-immunological research would substantially increase our knowledge about the plasticity and conservation of immune responses in a variety of different animals and conditions (Peuß et al., 2020).

69

70

71

72

73

74

75

76

77

78

79

80

81

82

83

84

85

86

87

88

89

90

To make sophisticated cellular composition analysis available to any research organism without the need for either pre-existing knowledge about the cell populations or species-specific reagents, we developed Image-Cytometry Cell Classification (Image3C). This method analyzes, visualizes, and quantifies, in a high-throughput and unbiased way, the composition of cell populations by using cell morphological traits and non-species-specific fluorescent probes (e.g., nuclear staining or dyes for metabolic states that function well in a variety of organisms) (Figure 1; Table 1). By taking advantage of cell morphology and/or fluorescent dyes related to function or metabolic state, Image3C can analyze single cell suspensions derived from any experimental design, de novo cluster cells present in the sample of interest and compare their abundance between each other or among different assays. Once the de novo clustering based on cell intrinsic features is obtained, Image3C employs a CNN that uses these clusters as training sets, avoiding in this way user bias or manual classification (Figure 1; Table 1). This produces a CNN-based cell classifier 'machine' used to quantify subsequently acquired image-based flow cytometry data and to compare cellular composition of samples across multiple experiments, in a highthroughput manner without the need for repeating time-consuming steps for *de novo* clustering. The combination of the clustered cell images, the outputs of their functional assays and the published literature about closely related organisms might allow the identification and description of cell types of interest. In comparison to existing label-free cell clustering methods, Image3C does not require initial antibody staining (Cheng et al., 2021; Hennig et al., 2017; Lippeveld et al., 2020; Nassar et al., 2019), pre-existing knowledge of specific cell morphology (Suzuki et al., 2019; Yakimov et al., 2019) and is not limited to a specific cellular phenotype (Blasi et al., 2016) for a priori identification of certain cell types (Table 1). This makes Image3C extremely versatile and applicable to virtually any research organism and tissue from which

92

93

94

95

96

97

98

99

100

101

102

103

104

105

106

107

108

109

110

111

112

113

dissociated single cells can be obtained. Parallelly to this *de novo* clustering approach, Image3C can take advantage of species-specific reagents and prior knowledge to be combined with transcriptomic dataset and provide a new and complimentary layer of information based on cell morphology and function. In sum, Image3C combines modern high-throughput data acquisition by image-based flow cytometry, advanced and unbiased clustering analysis, statistics to compare cellular compositions across different samples and a CNN classifier component to easily determine changes in cell composition across multiple experiments.

Results and Discussion

Image-Cytometry Cell Classification (Image3C)

Image3C is an imaging tool developed to study tissue composition at single-cell resolution in research organisms for which antibodies and pre-existing knowledge about cell types are not readily available (Figure 1; Table 1). Image3C allows for high-throughput and unbiased analysis in scenarios where manual counting and observer-based cell identification are currently the only options. Image3C includes all the components required for compensating captured images, quantifying multiple features for each event, clustering the events, visualizing and exploring the data, training and using the CNN for analyzing subsequent samples and integrating multiple experiments (Figure 1; Figure1-figure supplement 1).

Once a single-cell suspension is prepared from the organism of interest, the cells are stained with a combination of dyes that are expected to function independently irrespective of the species used, and which have high affinity for specific cellular organelles such as nuclei, or molecules associated with metabolic states such as reactive oxygen species. We validated reagents experimentally by determining that nuclear dyes stain intracellular material matching

expected characteristics of nuclear DNA or by activation of cells with drugs to change their metabolic state. The labelled samples are then run on the ImageStream® Mark II (Amnis Millipore Sigma) (Figure 1A). ImageStream is a commercially available image-based flow-cytometer, whose diffusion in laboratory settings is increasing and that provides highly reproducible images of cells that can be compared across days of acquisitions and experiments. For this approach, no microfluidic devices or custom-made and highly specialized microscopes are required (Table 1), but, if desired, the users can test the Image3C pipeline also on images acquired at standards microscopes, remembering to carefully control for batch effects.

Once images of individual events are collected for each channel of interest, feature values from both morphological and fluorescent data, such as cell size and nuclear size, are extracted from the cell images using IDEAS software (Amnis Millipore, free for download upon creation of Amnis user account) (Figure 1B; Supplementary File 1,2 for feature description). Correlation between features is calculated and redundant features are trimmed as well as samples that, among replicates, are outliers (Figure 2-figure supplement 1,2). This prevents clustering artifacts potentially caused by having multiple features providing the same information or including samples that are not representative (Figure 1B). During this step, while the number of features was usually reduced significantly, the correlation between replicates was always high and outliers were rarely observed (Figure 2-figure supplement 1,2). Finally, fluorescence intensity features are transformed to improve homogeneity of variance of distributions and, if used, DNA staining is normalized to remove intensity drift between samples and thus align the 2N and 4N DNA content histogram peaks (Figure 1B; Figure 2-figure supplement 3).

Exported feature quantifications are used for clustering the events. Dimensionality reduction and visualization of clusters is achieved by generating force directed layout (FDL) graphs in the

VorteX clustering environment (Figure 1C) (free to install) (Samusik, Good, Spitzer, Davis, & Nolan, 2016). Cell images for events within each cluster can be visualized using FCS Express Plus together with custom R scripts (Figure 1D). These visualization tools and the cluster feature averages (*i.e.*, the mean value of each feature for each cluster) (Figure 1E) allow to explore the images of selected groups of events and the features that differ between cells belonging to separate clusters. If control and treatment samples are included, a statistical analysis using negative binomial regression to compare cell counts per cluster between samples is also available in the Image3C pipeline. This high-throughput and unbiased analysis provides a comprehensive understanding of a cell population composition at higher resolution than what is possible with traditional histological methods.

Once this pipeline is run on a first set of samples (e.g., homeostatic state) and the cell clusters are defined for the tissue of interest, the images and the relative clustering IDs can be used to train a CNN classifier in an unbiased way (Figure 1F), including the ability to score frequency of "new" cell types that do not match any of the clusters identified at homeostasis. Therefore, future experiments in the same tissue used for training the CNN classifier can be analyzed directly through the CNN (Figure 1G). This significantly reduces the number of steps and time required to process data collected from following experiments with treated conditions. An even greater advantage is represented by the fact that, in the absence of CNN, every time new experimental sets are run it would be necessary to go again through the *de novo* clustering part of the pipeline (Figure 1B-E) and the new set of clusters would need to be cross-annotated to be compared with cell population composition observed in previous experiments. Manually matching clusters between different experimental sets might be a source of mistakes, mainly if the user is not familiar with the cell types present in the sample and if specific biomarkers or pre-existing

knowledge about cell types and morphology are not available. The CNN splits all the cell images in the classes defined during the training step and allows to compare the abundance of cells with same morphology among different samples without the need to cross-annotate clusters (Figure 1F,G). The CNN inclusion in Image3C and the reproducibility of image acquisition through image-based flow cytometry allows use of the clusters defined from one experiment (e.g., homeostatic state) to setup a classifier in an unbiased way for later use as a reference in analyzing experimental manipulations of these cell populations. We conclude from these results that Image3C can perform *de novo* high-throughput characterizations and define specific cell type behavior or population composition in both homeostatic and experimentally perturbed cell populations across multiple experiments.

Image3C recapitulates cell composition of zebrafish whole kidney marrow (WKM) tissue

To test whether Image3C could identify homogeneous and biologically meaningful cell populations, we used the research organism *Danio rerio*. We obtained cells from adult female zebrafish WKM (location of the hematopoietic tissue) in homeostasis condition, stained them and run on the ImageStream®^X Mark II. We analyzed intrinsic morphological and fluorescent features, such as cell and nuclear size, shape and darkfield signal (side scatter, SSC). Feature values were extracted from each cell image and processed through our pipeline (Supplementary File 1 for feature description). Clustering by the final set of normalized and non-redundant morphological and fluorescent features produced distinct cell populations (Figure 2A-C; Figure 2-figure supplement 1-3).

Image3C can distinguish between the major classes of cells present in zebrafish WKM (Figure 2; Supplementary File 3,4) that were described using standard sorting flow cytometry and

morphological staining approaches (D. Traver et al., 2003). It is noteworthy that Image3C can clearly identify dead cells and debris (Figure 2A,B) allowing to optimize experimental protocols in order to minimize cell death and to run the subsequent analysis only on the intact, live cells. Image3C can identify cells with outstanding morphological features, such as neutrophils from other myelomonocytes (Figure 2B,C). Based on zebrafish neutrophil characteristics such as high granularity, high complexity and low circularity of the nuclei (Lugo-Villarino et al., 2010), this type of granulocytes can be easily distinguished. Other types of myelomonocytes, such as monocytes and eosinophils are here merged in the same cluster, since in zebrafish they share many morphological characteristics (Lugo-Villarino et al., 2010). Similarly, using only intrinsic morphological features for the clustering, different lymphocytes (B and T-cells) and hematopoietic stem cells cannot be separated from each other, but they can be clearly distinguished from the myelomonocytes (Figure 2A,B). Within the Lymphocytes/Progenitors fraction we find two clusters (Dr1 and Dr7) that mainly differ in cell diameter (Figure 2C). Whether this morphological difference has a biological implication needs to be studied in future experiments. Image3C also enables the quantification of cell population (clusters or CNN classes) relative abundance, an important tool for comparing population composition across different treatment groups under different environmental conditions (Peuß et al., 2020). Here, we compared our results with previously published data to validate our method. Although a direct comparison with results from classical approaches (David Traver et al., 2003) is not possible since we gated out (removed analytically) mature erythrocytes before clustering (Material and Methods), the myelomonocyte to lymphocyte ratio (M/L ratio = 1.59) is similar to the one obtained with classic histological approaches (mean M/L ratio = 1.35) (Figure 2D) (David Traver et al., 2003).

207

208

209

210

211

212

213

214

215

216

217

218

219

220

221

222

223

224

225

226

227

228

231

232

233

234

235

236

237

238

239

240

241

242

243

244

245

246

247

248

249

250

251

252

Image3C identifies professional phagocytes in zebrafish WKM tissue

Next, we sought to determine whether Image3C could be used to characterize and quantify biological processes by identifying a tissue of interest and then comparing cellular composition dynamic, function, and physiological responses of specific cell types across a range of experimental conditions. Our goal was to detect statistically significant changes in cluster relative abundance between control and treated samples to gain a more detailed understanding of cell population dynamics and individual cell function.

As proof-of-concept, we performed a standard phagocytosis assay using WKM tissue from adult zebrafish. The single cell suspension was incubated with CellTrace Violet labeled Staphylococcus aureus (CTV-S. aureus) and with dihydrorhodamine-123 (DHR), a reactive oxygen species that becomes fluorescent if oxidized to report oxidative bursting following phagocytosis. As controls, we inhibited phagocytosis through cytoskeletal impairment with CCB incubation or through incubation with bacteria at lowered temperature by placing culture plates on ice. Events collected on the ImageStream®X Mark II were analyzed with Image3C and clustered in 26 distinct clusters using quantifications of morphological and fluorescent features (Supplementary File 2 for feature description), including nuclear staining, phagocytized S. aureus and DHR positivity (Figure 3A; Figure 3-figure supplement 1). Professional phagocytes are defined by their ability to take up S. aureus (CTV staining lies within the cell boundary) and induce a reactive oxygen species (ROS) response (bright DHR signal) (Rabinovitch, 1995). In zebrafish, professional phagocytes are mainly granulocytes and monocytic cells and can be discriminated from each other based on morphological differences, such as cell size, granularity and nuclear shape (Wittamer, Bertrand, Gutschow, & Traver, 2011). To compare samples

incubated with CTV-S. aureus and the samples where phagocytosis is inhibited (CTV-S. aureus + CCB and CTV-S. aureus + Ice), we used the statistical analysis included in Image3C based on a negative binomial regression model (Figure 3B,C; Figure 3-figure supplement 2; Supplementary File 5,6). Statistical analyses reported clusters with differences in relative abundance between phagocytosis and phagocytosis-inhibited samples. Visualizing these clustered event images (Supplementary File 7) while considering the values and intensities of morphological and fluorescent features for these clusters (Supplementary File 3) allowed identification of 4 clusters of professional phagocytes: granulocytes within clusters Dr4 P, Dr12 P and Dr13 P and monocytic cells in cluster Dr21 P (Figure 3A,B). The morphology of cells in cluster Dr12 P is characteristic of phagocytic neutrophils (Figure 2B; Figure 3A) that become adhesive and produce extracellular traps upon recognition of bacterial antigens (Palić, Andreasen, Ostojić, Tell, & Roth, 2007). Overall, the relative abundance of professional phagocytes is 5-10% (Figure 3C), which is in line with previous studies that estimated the number of professional phagocytes in WKM tissue of adult zebrafish using classical morphological approaches (Wittamer et al., 2011). It is also noteworthy that in line with other studies (Page et al., 2013), we did not observe a cluster of lymphocytes (e.g., B-cells) that actively phagocytize CTV-S. aureus bacteria (Figure 2; Supplementary File 7). Compared to the classical morphological approaches, Image3C allows to analyze thousands of events in a highthroughput and unbiased fashion, allowing the study of rare cell morphology and increasing results confidence and reproducibility. These results show that Image3C can successfully analyze biological processes since we were able to recapitulate the presence, cell type and frequency of professional phagocytes in adult zebrafish WKM organ.

253

254

255

256

257

258

259

260

261

262

263

264

265

266

267

268

269

270

271

272

273

A new aspect that Image3C highlighted is that CCB selectively affects cell viability based on cell identity, introducing artifacts and cell damage, actions not specific to inhibition of phagocytosis (Figure 3B). All mature erythrocyte containing clusters had a significantly higher cell count in the CTV-S. aureus samples compared to the CTV-S. aureus + CCB ones (Figure 3B; Supplementary File 3,5). Cluster analysis revealed that erythrocytes were almost absent in samples incubated with CCB (Supplementary File 3), while there was a significant increase in the relative abundance of clusters containing dead and apoptotic cells (Figure 3B; Supplementary File 5). Both outcomes are likely due to reduced cell viability of erythrocytes upon CCB incubation. Moreover, we excluded the possibility of higher cell death in the professional phagocytes upon CCB incubation, since pseudo-phagocytes (phagocytes with DHR response but no internalized CTV-S. aureus) were significantly more abundant in the CTV-S. aureus + CCB sample (Figure 3B; Supplementary File 5). These results are remarkable since Image3C allowed us to observe a specific effect of CCB on erythrocytes viability in zebrafish that, as far as we know, was not described before. Image3C analysis also uncover another important biological observation. When we inhibited phagocytosis by incubating the single cell suspension on ice (CTV-S. aureus + Ice) and compared the specificity of inhibition with the CTV-S. aureus + CCB sample (Figure 3C; Supplementary File 6), we discovered that the inhibition of phagocytosis through low temperature only affects adhesive neutrophils (cluster Dr12 P) (Figure 3C). This is suspected to occur as ice inhibits adhesion, while CCB effectively blocks phagocytosis in all professional phagocytes in zebrafish WKM tissue by acting on the cytoskeleton. The use of Image3C allowed us to specifically identify cell types that are sensible to low temperature and those that are not, confirming the existence of different phagocytosis mechanisms and providing additional

275

276

277

278

279

280

281

282

283

284

285

286

287

288

289

290

291

292

293

294

295

296

knowledge about pro and cons of different protocols that can be applied to inhibit phagocytosis based on specific goals and needs.

300

301

302

303

304

305

306

307

308

309

310

311

312

313

314

315

316

317

318

319

320

298

299

Image3C recapitulates cell composition of a freshwater snail hemolymph

Since we aim to provide a tool that is widely applicable, we tested Image3C versatility on the apple snail P. canaliculata an emerging organism for which molecular and cell biological tools have yet to be fully developed. As such, we repeated the same experiments done in zebrafish on the hemolymph of *P. canaliculata*. For morphological examination of the cellular composition of the hemolymph collected from female adults in homeostasis conditions, we stained the single cell suspensions with Drag5 (DNA dve) and ran on the ImageStream®X Mark II. We used Image3C to analyze the images of the events and we identified 9 cell clusters (Figure 4A; Figure 4-figure supplement 1). Two of these clusters were comprised of cell doublets, debris and dead cells (clusters Pc5 and Pc8) and the other clusters, based on inspection of cell images, were grouped into 2 main categories (Figure 4A; Supplementary File 8). The first category includes small blast-like cells (cluster Pc4) and intermediate cells (clusters Pc2 and Pc3) with high nuclear-cytoplasmic (N/C) ratio. These cells morphologically resemble the Group I hemocytes previously described using a classical morphological approach (Accorsi, Bucci, de Eguileor, Ottaviani, & Malagoli, 2013). The second category was comprised of larger cells with lower N/C ratio and abundant membrane protrusions (clusters Pc1, Pc6, Pc7 and Pc9). Likely, these cells correspond to the previously described Group II hemocytes that include both granular and agranular cells (Accorsi et al., 2013).

To identify which of these clusters were enriched for granular cells, we looked at the heatmap with feature values for each individual cluster (Figure 4B; Supplementary File 1 for feature

description). Cluster Pc6 had the highest values for the features related to cytoplasm texture and granularity (i.e., area granularity, intensity granularity and signal granularity) amongst all clusters other than cell doublets (Figure 4B; Supplementary File 3.8). Based on these data, we identified cluster Pc6 as the one containing the granular hemocytes. The clusters obtained by Image3C were not only homogeneous and biologically meaningful but were also consistent with published P. canaliculata hemocyte classification obtained by classical morphological methods (Accorsi et al., 2013). Such remarkable consistency was observed both in terms of identified cell morphologies and their relative abundance in the population of circulating hemocytes (Figure 4C; Supplementary File 8). For example, the relative abundance of the previously reported small blast-like cells is 14.0%, a value almost identical to the abundance of the corresponding cluster *Pc*4 (13.8%). Similarly, the category of larger hemocytes, or Group II hemocytes represents 80.4% of the circulating cells as measured by traditional morphological methods, while clusters Pc1, Pc6, Pc7 and Pc9 combined represent 72.4% of the events analyzed with Image3C (Figure 4C; Supplementary File 3). A sub-set of these cells are the granular cells (cluster Pc6), which correspond to 7.7% of all hemocytes by classical histological methods and 8.9% by Image3C. The intermediate cells (clusters Pc2 and Pc3) are less well represented in both approaches, with a relative difference in abundance of 5.6% versus 10.6% of the manually and Image3C analyzed events, respectively (Figure 4C; Supplementary File 3). This difference is likely best explained by the remarkable difference in both the number of cells and the number of features that can be considered for analysis by Image3C. Only a few hundred hemocytes were visually analyzed using traditional histological methods based only on cell diameter and N/C ratio (Accorsi et al., 2013). In contrast, the automated pipeline used by Image3C facilitated the analysis of 10,000

321

322

323

324

325

326

327

328

329

330

331

332

333

334

335

336

337

338

339

340

341

342

nucleated events for each sample and considered 25 morphological features for each cell. The significantly higher number of morphological features simultaneously considered by Image3C also explains the higher number of clusters and improved resolution to distinguish cell types compared to the traditional methods. Hence, Image3C, not only can properly analyze cells obtained from an emerging research organism generating biologically meaningful and informative clusters but also represents an unprecedented increase in the accuracy of cell type identification over traditional histological methods, while also allowing high-throughput capability.

Image3C identifies phagocytosis competent cells in the hemolymph of a freshwater snail

As with zebrafish, we also performed a phagocytosis experiment on hemocytes from *P. canaliculata*. Our goal was to test if it is possible with an emerging research organism to successfully discover cell phenotypes and functions and to obtain information about specific biological processes of interest by using Image3C to compare cell populations among treated and control samples.

Here, we setup the phagocytosis assay incubating the cells with CTV-*S. aureus* and DHR at room temperature. The phagocytosis was inhibited, as control, either adding EDTA (CTV-*S. aureus* + EDTA) or using low temperature by incubating samples on ice (CTV-*S. aureus* + Ice). Events collected on the ImageStream®^X Mark II were analyzed with Image3C and clustered in 20 distinct clusters using quantifications of morphological and fluorescent features (Supplementary File 2 for feature description), including nuclear staining, phagocytized *S. aureus* and DHR positivity (Figure 5A; Figure 5-figure supplement 1). We compared the phagocytosis permissive samples (CTV-*S. aureus*) with samples where phagocytosis was

inhibited by EDTA incubation or low temperature using the statistical analysis included in Image3C based on a negative binomial regression model (Figure 5B,C; Figure 5-figure supplement 2; Supplementary File 9,10). The clusters with relative abundance significantly higher in the phagocytosis samples (Figure 5B; Supplementary File 3,11) and with high intensities of both DHR and bacteria signals (Figure 5-figure supplement 3,4), are the two clusters that we identify as enriched with professional phagocyte (cluster Pc5 P and Pc17 P) (Figure 5B; Figure 4-figure supplement 1; Figure 5-figure supplement 4; Supplementary File 11). The two clusters show a different DHR signal intensity (ROS response) from one another upon bacteria exposure (cluster Pc5 P with high DHR signal, cluster Pc17 P with low DHR signal) (Figure 5-figure supplement 3; Supplementary File 3,11). Both Pc5 P and Pc17 P relative abundance is significantly higher in the phagocytosis samples compared to the EDTA treated sample (Figure 5C; Supplementary File 9), showing that EDTA effectively inhibits phagocytosis for both types of professional phagocytes. In the sample where the phagocytosis was inhibited by low temperature, however, only cluster Pc17_P had a significantly lower relative abundance compared to the phagocytosis sample (Figure 5C; Figure 3-figure supplement 2; Supplementary File 10). We can conclude that similar to CCB inhibition in the zebrafish phagocytosis experiment, EDTA is a more effective and generalized (not cell-type-specific) inhibitor of phagocytosis than low temperature. These results show that also in an emerging research organism, Image3C allowed discovery of new aspects of this biological process and highlighted differences among professional phagocytes that would have been difficult to detect with other methods.

367

368

369

370

371

372

373

374

375

376

377

378

379

380

381

382

383

384

385

386

387

388

389

The data analysis with Image3C clearly highlighted that CCB and EDTA, two classical phagocytic inhibitors commonly used in controls for phagocytosis experiments in vertebrates and

invertebrates, respectively, result in a drastic change of cell morphology and cell viability. This consequence is not easily detectable by other methods and is therefore often overlooked. In the present work, these changes significantly modified the overall cell cluster number and distribution and indicates that the effects of CCB and EDTA on cell morphology should be taken into consideration in any study of morphological features of cells with phagocytosis properties because artifacts might be significant.

Convolutional Neural Network (CNN) allows unbiased comparison between experiments

When determining differences between control and experimental treatments, Image3C necessarily combines images and data from all samples and then clusters the cells. This must be taken into consideration for experimental planning. Experiments meant to analyze cell composition and morphological diversity in one biological domain (*e.g.*, homeostasis condition) (Figure 2; Figure 4) should be carried out separately from those in other domains that are likely to introduce changes in the cell population composition or cell morphologies that would be a confounding factor for the *de novo* clustering in homeostasis condition. Image3C clustering works best when used, at the same time, only on samples belonging to a single experimental domain, such as homeostasis or the phagocytosis assay. An issue that emerges when analyzing different experimental sets independently is the increase of time requirement for analytical steps, the likelihood of introducing errors, and the need to repeatedly annotate the clusters in the FDL graph obtained from each experimental set. This last element is required for comparing cell type behaviors among multiple experiments and have a global understanding of their functions and response to treatments (*i.e.*, cluster #1 from one analytical run cannot be expected to match cell

morphologies with cluster #1 from another run, since there is a stochastic element to the process).

This last point is probably the most challenging since mistakes can easily be introduced based on user-biases or lack of sufficient pre-existing knowledge about cell morphologies or of cell biomarkers that would allow a confident cross-annotation between multiple FDL graphs. In addition, we observed that the number of clusters drastically increases when including treatments that influence cell morphological properties of the cell. As an example, while we detected 9 unique clusters in naïve hemolymph samples, we detected 20 clusters in the phagocytosis experiment (Figure 3A; Figure 4A). This is in part due to the fact that professional phagocytes change their morphology upon detection of pathogens (Palić et al., 2007), thus creating new clusters. Similarly, the complexity of the clustering is also increased by treatments, such as CCB and EDTA incubations, that are necessary to ensure identification of professional phagocytes, but have a strong impact on the morphology of the cells making the clustering and annotation steps more challenging and prone to mistakes since treated samples contain aberrant populations not found at homeostasis (Figure 5A; Supplementary File 11).

To provide an alternative for streamlining the analysis of multiple experimental sets upon initial *de novo* clustering and cell type identification in homeostasis samples, we included in Image3C the possibility to use these initial images and their cluster IDs to train a CNN without manually classifying the images (Figure 1). This trained classifier can then be used to assign the cell images subsequently collected from additional experimental sets to one of the clusters defined in the homeostasis condition in a high-throughput way. In this way it will be possible to determine the behavior of a specific cell type through multiple experimental sets without reclustering whenever new data is acquired. A crucial element that allows this approach is also

represented by the ImageStream®^X Mark II system that provides highly reproducible and comparable images of cells coming from different experiments and acquired in different days, introducing much less variability then standard light or electron microscopy.

435

436

437

438

439

440

441

442

443

444

445

446

447

448

449

450

451

452

453

454

455

456

457

For our pipeline, then, a CNN (LeCun et al., 1989) based on the architecture of DenseNet (Huang, Liu, Maaten, & Weinberger, 2017) was deployed to: 1. use, as training set, images and clusters obtained from a first group of samples (e.g., homeostasis conditions, naïve cells or WT samples) analyzed in an unbiased way by de novo clustering and 2. assign new cell images acquired through ImageStream®X Mark II system to their respective classes. As proof-ofconcept, we used the clusters identified for P. canaliculata hemocytes in homeostasis condition with the first part of the pipeline (Figure 4A) for training and setting up the CNN classifier. This approach would define the classes based on the unbiased *de novo* clustering of thousands of cells with no need for formal annotation or previous knowledge about cell types and tissue composition. To prepare a data set for training the classifier, we first combined clusters that strongly overlapped with one another in terms of morphological characteristics (e.g., doublets and dead cells) to increase accuracy of the classifier (Figure 6A). We used 80% of the cells obtained in the original P. canaliculata dataset together with their cluster IDs to train the classifier through over 25,000 iterations. After each iteration, we tested the training with 10% of the original dataset and we determined the relative accuracy by scoring numbers of cells whose cluster ID assigned by the classifier matched the original cluster ID (Figure 6B,C). The remaining 10% of the original dataset was used to calculate the precision of the trained classifier. Clusters with higher support numbers obtained higher precision scores. The weighted average precision score (f1-score, precision average score across clusters controlling for support numbers) of 0.75 is relatively high considering the complexity of the phenotype (BF, darkfield

and Draq5 images) (Figure 6D) and comparable to other studies using machine learning for cell classification (Blasi et al., 2016). The true probability match for each individual cell (probability for each cell that the class assigned by the classifier would match the original cluster ID) demonstrated that lower true probability matches occurred where clusters strongly overlapped or where cell phenotypes are intermediate between clusters, providing an additional layer of information about our dataset (Figure 6D).

To test the efficiency of this pipeline, we extracted all the images belonging to the two clusters identified in the phagocytosis assay as cluster-containing phagocytes and determined to

458

459

460

461

462

463

464

465

466

467

468

469

470

471

472

473

474

475

476

477

478

479

480

which naïve cell-type they correspond using the CNN classifier and only the BF, SSC and Drag5 channels (i.e., DHR and labeled bacteria signals where not used). We found that 59.4%, 6.2% and 9.2% of the phagocytes belonged to cluster Pc1 CT, Pc6 CT and Pc7 CT, respectively (Figure 6E), where CT stands for Classifier Training. These results confirmed a previously published result that used classical morphological staining and manual annotation to conclude that the hemocytes able to phagocytize were primarily Group II hemocytes (Accorsi et al., 2013). Only 8% of the phagocytes were clustered in the Group I hemocytes, here represented by cluster Pc2 CT, Pc3 CT and Pc4 CT, while the remaining 17.2% were assigned by the CNN to the cluster Pc5 CT, constituted by doublets and dead cells (Figure 6E). This result can be explained by the fact that in vitro phagocytosis triggers microaggregate formation (hemocyte-hemocyte adhesion) in invertebrate hemocytes that resembles the nodule formation observed in vivo (Walters, 1970). It is important to observe how this analysis allowed us to assign phagocytes to cell types using the annotation already performed in Figure 4A (de novo clustering of hemocytes in homeostasis condition) without the need to re-annotate the FDL obtained during the phagocytosis assay (Figure 5A).

To test the adaptability of the trained CNN to new datasets, we collected hemocytes from male apple snail specimens, we stained the cells with Drag5 and recorded BF, SSC and nuclei images from 10,000 cells on the ImageStream®^X Mark II as previously described. We extracted the images of the cells, and we used the trained CNN classifier to determine the relative abundance of hemocytes collected from male snails in the 7 classes of the classifier (Figure 6F). First, we visually compared the female hemocytes clustered by the *de novo* clustering with the male hemocytes that were run on the ImageStream®^X Mark II and were assigned to a class by the classifier (Figure 6F). This comparison shows that the female and male hemocytes belonging to the same cluster are morphologically extremely similar and different from the hemocytes assigned to other clusters (Figure 6F). This demonstrates that the CNN classifier can be trained with a first group of samples and then it can successfully analyze new datasets acquired later on. The comparison between female and male hemocyte compositions revealed that the clusters significantly different in terms of relative abundance are Pc1 CT and Pc7 CT (Group II agranular large hemocytes) and Pc6 CT (Group II granular large hemocytes) (Figure 6F). Significantly, prior studies detected no differences between females and males hemocytes composition through manual classification and counting using a classical morphological approach (Accorsi et al., 2013). The user-bias-free and high-throughput analysis presented here, in contrast, allowed us to determine that one of the two subpopulations of agranular large hemocytes was significantly more abundant in the female animals (Pc1 CT: 53% and 38% in females and males, respectively) while the other agranular (Pc7 CT) as well as the granular large hemocytes (Pc6 CT) was significantly more abundant in the male animals (Pc7 CT: 14% and 20% in females and males, respectively; Pc6 CT: 6% and 10% in females and males, respectively) (Figure 6F).

481

482

483

484

485

486

487

488

489

490

491

492

493

494

495

496

497

498

499

500

501

502

While the biological significance of this observation is not going to be further investigated in this paper, the discovery highlights the power of Image3C analysis compared to traditional methods for determining and quantitating the composition of cell populations. These experiments demonstrate that Image3C, in combination with the presented convolutional classifier, can analyze large experimental datasets and identifying significances with small effect sizes. Importantly, Image3C analysis is independent of observer biases and does not require prior knowledge about expected tissue composition or the expected effect of treatment on cell morphology.

Conclusion

We have developed a powerful new method to analyze at single-cell resolution the composition of any cell population obtained from research organisms for which species-specific reagents (such as fluorescently tagged antibodies), biomarkers, single-cell atlases or a high-quality genome for a scRNA-Seq approach are not available. We demonstrated that Image3C can identify different cell populations based on morphology and/or function through *de novo* clustering and highlight important changes in cell type abundance and cell population composition caused by experimental or natural perturbation (sex, treatment, experimental protocol). Image3C does not require, at any point, prior knowledge about the tissue composition or cell type specific markers, although, if available, they can be included and used. Furthermore, in combination with the CNN classifier trained on these clusters, we demonstrate that Image3C is capable of bias-free and high-throughput analysis of large experimental datasets making it possible to compare a specific cell type behavior or population composition across multiple experiments. Image3C is extremely versatile and can be applied to any tissue or cell population

of interest and is adaptable to a variety of experimental designs. Although, Image3C was develop in response to the need of analyzing cell composition of tissues in emerging research organisms, the Image3C tool could be potentially used also to add to transcriptomic dataset an additional and complementary layer of information based on cell morphology. Given the recent advancement in image-based flow cytometry that enables image capturing together with cell sorting (Nitta et al., 2018), a scRNA-Seq approach in combination with the Image3C pipeline would enable simultaneous analysis of both the morphological/phenotypic and genetic properties of a cell population at single cell resolution.

536 Materials and Methods

Key Resources Table				
Reagent type (species) or resource	Designation	Source or reference	Identifiers	Additional information
strain, strain background (Staphylococcus aureus)	Wood strain without protein A	Thermo Fisher Scientific	S2859	
biological sample (<i>Danio reri</i> o)	Whole kidney marrow	Stowers Institute for Medical Research	Wild type, Adult females	Freshly isolated from <i>Danio rerio</i>
biological sample (<i>Pomacea</i> <i>canaliculata</i>)	Hemolymph	Stowers Institute for Medical Reserach	Wild type, Adult females and males	Freshly isolated from <i>Pomacea</i> canaliculata
chemical compound, drug	Dihydrorhoda mine-123 (DHR)	Thermo Fisher Scientific	D23806	5 uM
software, algorithm	IDEAS	Amnis Millipore Sigma	Version 6.2	
software, algorithm	R code	This paper		https://github.co m/stowersinstitu te/LIBPB-1390- Image3C
software, algorithm	VorteX clustering environment	https://github.co m/nolanlab/vort ex/releases		
software, algorithm	FSC Express	De Novo Software	Image or Plus configuration s - Version 7	
software, algorithm	Python script	This paper		https://github.co m/stowersinstitu te/LIBPB-1390- Image3C
other	Draq5	Thermo Fisher Scientific	62251	5 uM
other	CellTrace Violet	Thermo Fisher Scientific	C34571	5 uM

Collection of zebrafish whole kidney marrow (WKM)

Twelve-month-old, wild type, female, adult zebrafish were euthanized with cold 500 mg/L MS-222 solution for 5 min. WKM was dissected as previously described (D. Traver et al., 2003) and transferred to 40 µm cell strainer with 1 mL of L-15 media containing 10% water, 10 mM HEPES and 20 U/mL Heparin (L-90). Cells were gently forced through the cell strainer with the plunger of a 3 mL disposable syringe. The strainer was washed once with 1 mL of L-90 and the resulting single cell suspension was centrifuged at 500 rcf at 4 °C for 5 min. The supernatant was discarded, and the cells were resuspended in 1 mL of L-90 containing 5% fetal calf serum (FCS), 4 mM L-Glutamine, and 10,000 U of both Penicillin and Streptomycin (L-90 media). The cells were counted in a 1:20 dilution on the EC-800 flow cytometer (Sony) using scatter properties.

Collection of apple snail hemocytes

Specimens of the apple snail *Pomacea canaliculata* (Mollusca, Gastropoda, Ampullariidae) were maintained and bred in captivity, in a water recirculation system filled with artificial freshwater (2.7 mM CaCl₂, 0.8 mM MgSO₄, 1.8 mM NaHCO₃, 1:5000 Remineralize Balanced Minerals in Liquid Form [Brightwell Aquatics]). The snails were fed twice a week and kept in a 10:14 light:dark cycle. Wild type adult snails, 7-9 months old and with a shell size of 45-60 mm were starved for 5 days before the hemolymph collection (Accorsi et al., 2013). If not differently specified, female snails were used for the experiments. The withdrawal was performed applying a pressure on the operculum and dropping the hemolymph directly into an ice-cold tube. The hemolymph collected from different animals was not pooled together. The hemolymph was immediately diluted 1:4 in Bge medium + 10% fetal bovine serum (FBS) and then centrifuged at 500 rcf for 5 min. The pellet of cells was resuspended in 100 μl of Bge medium + 10% FBS. The

Bge medium (also known as *Biomphalaria glabrata* embryonic cell line medium) is constituted by 22% (v/v) Schneiders's Drosophila Medium, 4.5 g/L Lactalbumin hydrolysate, 1.3 g/L Galactose, 0.02 g/L Gentamycin in MilliQ water, pH 7.0.

Experiment 1: Morphology Assay in homeostasis conditions

WKM cells from zebrafish were isolated as described before and plated at 4×10^5 cells/well in a 96-well plate in 200 μ L of L-90 media and incubated for 3 h at room temperature. Cells were stained with 5 μ M Draq5 (Thermo Fisher Scientific) for 10 min and subsequently run on the ImageStream® Mark II (Amnis Millipore Sigma), where 10,000 nucleated and focused events were recorded for each sample (n=8). Erythrocytes were out-gated to enrich for immune relevant cells and to prevent over-clustering in the subsequent analysis. The latter is due to the fact that fish erythrocytes are nucleated and their biconcave shape results in different morphological feature values only depending on their orientation during image acquisition.

The *P. canaliculata* hemocytes were stained with 5 μ M Draq5 (Thermo Fisher Scientific) for 10 min, moved to ice and subsequently run on the ImageStream®^X Mark II (Amnis Millipore Sigma), where 10,000 nucleated and focused events were imaged for each sample (n=5).

Experiment 2: Phagocytosis Assay

Staphylococcus aureus (Thermo Fisher Scientific) were resuspended in PBS at the final concentration of 100 mg/ml and incubated with 5 uM CellTrace Violet (CTV; Thermo Fisher Scientific) for 20 min. Labelled bacteria were centrifuged and resuspended in PBS for 3 times to remove unbound dye and then stored at -20 °C as single-use aliquots. Cells, obtained from fish WKM or snail hemolymph and in a single cell suspension, were plated in a 96-well plate at a

concentration of 4 x 10⁵ cells/well in 200 μL of medium and incubated with 2 x 10⁷ CTV-coupled *S. aureus*/well for 3 h at room temperature. As control, the phagocytosis was inhibited incubating the cells + CTV-*S. aureus* mix either on ice (for both species) or with 0.08 mg/mL cytochalasin B (CCB) for zebrafish cells or with 30 mM EDTA and 10 mM HEPES for apple snail cells (Cueto, Rodriguez, Vega, & Castro-Vazquez, 2015; Li et al., 2006). After 2 h and 30 min we added 5 μM dihydrorhodamine-123 (DHR) (Thermo Fisher Scientific) to the cell suspension to stain cells positive for reactive oxygen species (ROS) production. To control for this treatment with DHR, we incubated one aliquot of cells with 10 ng/mL phorbol 12-myristate 13-acetate (PMA) to induce ROS production. At 2 h and 50 min since the beginning of incubation with CTV-*S. aureus*, all the samples were stained with 5 μM Draq5 for 10 min. After 3 h incubation with bacteria, cells were moved and stored on ice and subsequently run on the ImageStream®^X Mark II (Amnis Millipore Sigma), where 10,000 nucleated and focused events were imaged for each sample (at least n=4 snail and n=6 fish) at a speed of 1,000 images/sec.

Data collection on ImageStream®^X Mark II

Following cell preparation, data were acquired from each sample on the ImageStream®^X Mark II (Amnis Millipore Sigma) at 60x magnification, slow/sensitive flow speed (1,000 images/sec), using 633, 488 and 405 nm laser excitation. Bright field was acquired on channels 1 and 9, DHR (488 nm excitation) on channel 2, CTV-*S. aureus* (405 nm excitation) on channel 7, Draq5 (633 nm excitation) on channel 11, and SSC was acquired on channel 6. Single color controls were also acquired for each fluorescent channel to allow for fluorescence spillover correction.

Data analysis and de novo cluster identification

606

607

608

609

610

611

612

613

614

615

616

617

618

619

620

621

622

623

624

625

626

627

628

An interactive map representing the pipeline, the software used, the format of the exported files and an approximation of time required for running the individual steps is provided in Figure 1-figure supplement 1. Raw images from the ImageStream®^X Mark II system (RIF files, a type of modified 16 bit TIFF file) were compensated (spillover and other corrections applied), background was subtracted, and features were calculated using IDEAS 6.2 software (Amnis Millipore, free for download once an Amnis user account is created). The resulting compensated image files (CIF files) were used to quantify features for all cells and samples. Supplementary File 1,2 report the list of features used for each organism and for each experiment and their description. These per-object feature matrices (DAF files) were then exported from IDEAS into FCS files. Exported FCS files were processed in R (R Core Team, 2014). In order to trim redundant features that contribute noise but little new information, Spearman's correlation values for each pair of features were calculated using all events of a representative sample and one of the features of the pair was trimmed when correlation was ≥ 0.85 for the pair (Figure 2-figure supplement 1) (Caicedo et al., 2017). The Spearman's correlation of the mean values of remaining features per each sample were then used to identify outliers among sample replicates. Samples with correlation of mean feature values below 0.85 with the set were discarded (Figure 2-figure supplement 2; Figure 3-figure supplement 1; Figure 4-figure supplement 1; Figure 5figure supplement 1), although in general the replicates were consistent. Also, while morphological features did not require any transformation or normalization, fluorescence intensity features were transformed using the estimateLogicle() and transform() functions from the R flowCore package (Ellis et al., 2018; Hahne et al., 2009) to improve homoscedasticity (homogeneity of variance) of distributions. DNA intensity features were also normalized to align

all 2N and 4N peak positions and to remove intensity drift between samples (Figure 2-figure supplement 3) using the gaussNorm() function from flowStats package (Hahne, Gopalakrishnan, Khodabakhshi, Wong, & Lee, 2018). The processed data was exported from R (R Core Team, 2014) using writeflowSet() function in flowCore package (Ellis et al., 2018; Hahne et al., 2009) as CSV or FCS files, depending on downstream needs for the file output.

629

630

631

632

633

634

635

636

637

638

639

640

641

642

643

644

645

646

647

648

649

650

651

These processed data files were then imported into the VorteX clustering environment for X-Shift k-nearest-neighbor clustering (free to install) (Samusik et al., 2016). X-Shift was selected as a clustering method for Image3C based on a previously published analysis and comparison of clustering methods (Weber & Robinson, 2016). From that work, we determined that X-shift represents an optimal trade-off: identifying low frequency populations, accurately identifying 'true' clusters (i.e., F1 scores), not requiring for a priori knowledge of the number of clusters (populations) and having reasonable runtimes (due to hardware CPU requirements). We also did an early comparison of X-shift with K-means (data not shown) and determined that K-means was insufficient for our purposes as known cell populations were not well represented by clusters, and we did not want to specify the number of expected clusters into the method's input parameters since this would not be known in experimental use. During the import into VorteX, all features were scaled to 1SD to equalize the contribution of features towards clustering. Clustering was performed in VorteX testing a range of k values (typically from 5 to 150), choosing a final k value using the 'find elbow point for cluster number' function in VorteX and confirming visually that over- or under-clustering did not occur. Force directed layout (FDL) graphs of a subset of cells obtained from each set of samples were also generated in VorteX and cell coordinates in the resultant 2D space were exported along with graphML representation of the FDL graph. Finally, tabular data (CSV files) was exported from VorteX including a master

table of every cell event with its cluster assignment and original sample ID, as well as a table of the average feature values for each cluster and counts of cells per cluster and per sample.

Clustering results were further analyzed and plotted in R (R Core Team, 2014) by merging all cell events and feature values with cluster assignments and X/Y coordinates for FDL graph. Using this merged data and the graphML file exported from VorteX, new FDL graphs were created for each treatment condition using the igraph package (Csardi & Nepusz, 2006) in R (R Core Team, 2014). Statistical analysis of differences in cell counts per cluster by condition were performed using negative binomial regression of cell counts per cluster, plots of statistic results and other results were generated, and CSV files containing cell ID, sample ID, feature values, X/Y coordinates in FDL graph were exported for each sample. The subsequent use of FCS Express Plus version 6 (DeNovo software, free alternative are mentioned later in the text) allowed visualization of cell images using DAF/CIF files by cluster and by customized subsets of the FDL graphs.

DAF files were opened in FCS Express Plus software and the "R add parameters" transformation feature with a custom script was used to merge the clustering data saved in the CSV files generated above with both DAF and CIF files (feature values and image sets, respectively). FCS Express Plus was utilized at this stage of work because it is the only platform currently available that works with Amnis DAF and CIF files while also running transformation processes driven by R scripting. ImageJ Bio-Formats allows reading images from DAF and CIF files but we got pixels with a value much higher than expected, probably due to a bug that has not been fixed, yet. This allowed to visualize image galleries of cells within each cluster and gate by features of interest on 2D plots (more traditional flow cytometry analysis) for exploring the clustering results and identifying clusters and populations of interest. FCS Express Plus is a

proprietary software, but similar results can be obtained with IDEAS software where a text file with cluster IDs for each image event can be imported and the cluster information can be matched to the event images.

The full complement of R packages used includes flowCore (Ellis et al., 2018; Hahne et al., 2009), flowStats (Hahne et al., 2018), igraph (Csardi & Nepusz, 2006), ggcyto (Jiang, 2015), ggridges (Wilke, 2018), ggplot2 (Wickham, 2016), stringr (Wickham, 2010), hmisc (Harrell & Dupont, 2019) and caret (Kuhn, 2008). Figure 1-supplement figure 1 can be used as an interactive map of Image3C pipeline, where, clicking on the different portions of the pipeline, the users will be automatically directed to the corresponding section of our GitHub repository. The GitHub repository at https://github.com/stowersinstitute/LIBPB-1390-Image3C reports a detailed description of all these processing steps and includes sample scripts, workflow files, example datasets and tutorials.

Setup and use of a Convolutional Neural Network (CNN) Classifier

Once the clusters were defined with the previously described *de novo* clustering analysis, we used a CNN (LeCun et al., 1989) based on the architecture of DenseNet (Huang et al., 2017) for image classification. Out of all the events captured with the ImageStream®^X Mark II system, we selected only single nucleated objects applying gates on area vs aspect ratio plot and Draq5 intensity plot to achieve this selection, respectively. For these objects, we exported 16 bit TIFF images (one channel per fluorescence/BrightField image 'color') using IDEAS 6.2 software (Amnis/Millipore, free for download once an Amnis user account is created).

Because images from the ImageStream®^X Mark II system have non-uniform sizes, each image was cropped or padded to 32x32 pixels using NumPy indexing (Walt, Colbert, &

Varoquaux, 2011) in a Python script. The CNN consists of three dense blocks that transition from three-channel image input of 32x32x3 to a final size of 4x4x87 with 87 feature maps. A dense block includes three convolution layers, each followed by leaky ReLU activation. The last step of the block is a strided convolution used to down-sample the width and height of the feature maps by a factor of 2. The final layer of the CNN flattens the 4x4x87 array into a 1D vector of length 1392 and is fully connected to the output layer that is a 1D vector with a length of the number of classes for prediction. The CNN used softmax cross entropy for the loss function with L2 regularization, and the Adam optimizer (Kingma & Ba, 2015) was used to minimize the loss function. The CNN was implemented in Python using the TensorFlow platform (Abadi et al., 2015) and the SciPy ecosystem (T. Oliphant, 2006; T. E. Oliphant, 2007; Pedregosa et al., 2011).

The CNN was used to train a classifier using over 35,000 images of P. canaliculata hemolymph cell types in homeostasis condition acquired with the ImageStream®X Mark II system. The event images were randomly split in 80% for training, 10% for testing during training, and 10% for final validation. The first 80% of the images were used together with their cluster IDs obtained by the *de novo* clustering to train the classifier. The learning rate for the Adam optimizer was set to 0.0006 with a decaying learning rate starting at 0.001 and decreasing by 1% each step. The training proceeded for 25,000 iterations with a size of 256 randomly selected images for each iteration. After each iteration, 10% of the cells of the original P. canaliculata dataset was used to test the classifier. The loss and accuracy of the CNN were recorded after every 100 iterations to monitor the performance. The CNN loss was defined by the softmax of the cross entropy (Dahal, 2017) between the final output and the one-hot-encoded image labels. To avoid the CNN memorizing the training set, L2 regularization was applied to

the weights. The training and test set follow the same accuracy and loss trends over all iterations indicating the training set is not memorized and can generalize to predict the test set.

The finally trained classifier was tested on the remaining 10% of images that were completely new for the CNN. The trained model was saved for future use, so new images can be inferred by the network to predict cell types. The inference is very fast because only one forward pass is made through the network and no back propagation occurs. The result of the inference is a vector with length equal to the number of cell type classes. Each element of the vector will be the probability of the cell belonging to the corresponding class; the sum of the vector must be 1. Inferring a complete experiment will provide a probability vector for each image; the list of probability vectors can be saved as CSV file. For new images, the inference results will need to be examined to ensure the predictions are reliable. A large majority of the probability vectors should have a maximum greater than 0.5, and a subset of the images should be visually inspected to verify proper class assignment.

The interactive map of Image3C pipeline (Figure 1-figure supplement 1) includes also the training and the of the CNN. The GitHub repository use at https://github.com/stowersinstitute/LIBPB-1390-Image3C reports a detailed description of all these processing steps, includes sample scripts, workflow files, example datasets and tutorials and can be easily accessed clicking on the right side of the Image3C interactive map (Figure 1figure supplement 1).

740

741

742

743

721

722

723

724

725

726

727

728

729

730

731

732

733

734

735

736

737

738

739

Statistical Analysis

Negative binomial regression was performed on tables of cell counts per cluster and per sample and plots were generated using R (R Core Team, 2014) with the edgeR package

(Robinson, McCarthy, & Smyth, 2010), which was developed for RNAseq analysis, but includes generally applicable and user-friendly wrappers for regression and modeling analysis and plotting of results. For the comparison of cellular hemolymph composition between females and males of *P. canaliculata* a one-way ANOVA with subsequent FDR (Benjamini-Hochberg, correction for multiple testing) was used.

751 <u>Acknowledgements</u>

752 We acknowledge Hua Li for her assistance on the statistical analysis and we also thank the 753 Laboratory Animal Services and the Aquatics Facility at the Stowers Institute for Medical 754 Research for animal husbandry. We would like to thank Blair Benham-Pyle, Carolyn Brewster, 755 Viraj Doddihal, Julia Peloggia de Castro and Barbara Milutinović for their critical comments on 756 an earlier version of this manuscript. This work was supported by institutional funding to ACB, 757 CW, ASA and NR. ASA is a Howard Hughes Medical Institute Investigator. NR is further 758 supported by the Edward Mallinckrodt Foundation, NIH Grant R01 GM127872, DP2AG071466 759 and NSF EDGE award 1923372. AA was supported by the Emerging Models grant from the 760 Society for Developmental Biology (SDB) and the postdoctoral fellowship from the American 761 Association of Anatomists (AAA). RP was supported by a grant from the Deutsche 762 Forschungsgemeinschaft (PE 2807/1-1).

763

764

Author Contributions

- AA, ACB and RP conceived and designed the study with input from ASA and NR. RP
- performed D. rerio experiments. AA performed P. canaliculata experiments. ACB conceived
- and wrote the Image3C pipeline and associated R-scripts. CW designed and optimized the
- convolutional neural network. AA, ACB, RP and CW analyzed and interpreted the data. AA,
- ACB and RP wrote the paper. All authors read and edited the paper.

770

771

Data availability statement

- All original data underlying this manuscript can be accessed from the Stowers Original Data
- Repository at http://www.stowers.org/research/publications/libpb-1390. Image3C code and

- 774 description, workflow files, example datasets, and tutorials are freely available at the GitHub
- 775 repository https://github.com/stowersinstitute/LIBPB-1390-Image3C.

776

- 777 Ethics statement
- 778 This study was performed in strict accordance with the recommendations in the Guide for the
- 779 Care and Use of Laboratory Animals of the National Institutes of Health. Research and animal
- 780 care were approved by the Institutional Animal Care and Use Committee (IACUC) protocol
- 781 (#2019-080) of the Stowers Institute for Medical Research.

782

- 783 Conflict of interest
- 784 The authors declare no conflict of interest.

785

791

792

793

794

795

796

797

798

- 786 References
- 787 Accorsi, A., Bucci, L., de Eguileor, M., Ottaviani, E., & Malagoli, D. (2013). Comparative analysis 788 of circulating hemocytes of the freshwater snail Pomacea canaliculata. Fish Shellfish 789 Immunol, 34(5), 1260-1268. doi:10.1016/j.fsi.2013.02.008
- 790 Baron, C. S., Barve, A., Muraro, M. J., van der Linden, R., Dharmadhikari, G., Lyubimova, A., . . . van Oudenaarden, A. (2019). Cell Type Purification by Single-Cell Transcriptome-Trained Sorting. Cell, 179(2), 527-542 e519. doi:10.1016/j.cell.2019.08.006
 - Blasi, T., Hennig, H., Summers, H. D., Theis, F. J., Cerveira, J., Patterson, J. O., ... Rees, P. (2016). Label-free cell cycle analysis for high-throughput imaging flow cytometry. Nat Commun, 7, 10256. doi:10.1038/ncomms10256
 - Caicedo, J. C., Cooper, S., Heigwer, F., Warchal, S., Qiu, P., Molnar, C., . . . Carpenter, A. E. (2017). Data-analysis strategies for image-based cell profiling. Nat Methods, 14(9), 849-863. doi:10.1038/nmeth.4397
- 799 Cheng, S., Fu, S., Kim, Y. M., Song, W., Li, Y., Xue, Y., . . . Tian, L. (2021). Single-cell 800 cytometry via multiplexed fluorescence prediction by label-free reflectance microscopy. 801 Sci Adv, 7(3). doi:10.1126/sciadv.abe0431
- 802 Csardi, G., & Nepusz, T. (2006). The igraph software package for complex network research. 803 InterJournal, Complex Systems, 1695(5), 1-9.
- 804 Cueto, J. A., Rodriguez, C., Vega, I. A., & Castro-Vazquez, A. (2015). Immune Defenses of the 805 Invasive Apple Snail Pomacea canaliculata (Caenogastropoda, Ampullariidae): 806 Phagocytic Hemocytes in the Circulation and the Kidney. PLoS One, 10(4), e0123964.

807 doi:10.1371/journal.pone.0123964

- 808 Ellis, B., Haaland, P., Hahne, F., Le Meur, N., Gopalakrishnan, N., Spidlen, J., & Jiang, M. (2018). flowCore: flowCore: Basic structures for flow cytometry data. R package version 1.46.1.
- Eulenberg, P., Kohler, N., Blasi, T., Filby, A., Carpenter, A. E., Rees, P., . . . Wolf, F. A. (2017).
 Reconstructing cell cycle and disease progression using deep learning. *Nat Commun,*8(1), 463. doi:10.1038/s41467-017-00623-3

- Goolam, M., Scialdone, A., Graham, S. J. L., Macaulay, I. C., Jedrusik, A., Hupalowska, A., . . . Zernicka-Goetz, M. (2016). Heterogeneity in Oct4 and Sox2 Targets Biases Cell Fate in 4-Cell Mouse Embryos. *Cell*, *165*(1), 61-74. doi:10.1016/j.cell.2016.01.047
- Hahne, F., Gopalakrishnan, N., Khodabakhshi, A. H., Wong, C., & Lee, K. (2018). flowStats: Statistical methods for the analysis of flow cytometry data. R package version 3.38.0.
- Hahne, F., LeMeur, N., Brinkman, R. R., Ellis, B., Haaland, P., Sarkar, D., . . . Gentleman, R. (2009). flowCore: a Bioconductor package for high throughput flow cytometry. *BMC Bioinformatics*, *10*, 106. doi:10.1186/1471-2105-10-106
- Harrell, F. E., & Dupont, C. (2019). Hmisc: Harrell Miscellaneous. Retrieved from http://biostat.mc.vanderbilt.edu/Hmisc
- Hennig, H., Rees, P., Blasi, T., Kamentsky, L., Hung, J., Dao, D., . . . Filby, A. (2017). An open-source solution for advanced imaging flow cytometry data analysis using machine learning. *Methods*, *112*, 201-210. doi:10.1016/j.ymeth.2016.08.018
- Huang, G., Liu, Z., Maaten, L. v. d., & Weinberger, K. Q. (2017, 21-26 July 2017). *Densely Connected Convolutional Networks*. Paper presented at the 2017 IEEE Conference on Computer Vision and Pattern Recognition (CVPR).
- Jiang, M. (2015). ggcyto: Visualize Cytometry data with ggplot. R package version 1.8.0.
- Kaczorowski, K. J., Shekhar, K., Nkulikiyimfura, D., Dekker, C. L., Maecker, H., Davis, M. M., . . Brodin, P. (2017). Continuous immunotypes describe human immune variation and predict diverse responses. *Proc Natl Acad Sci U S A, 114*(30), E6097-E6106. doi:10.1073/pnas.1705065114
- Kimmel, J. C., Penland, L., Rubinstein, N. D., Hendrickson, D. G., Kelley, D. R., & Rosenthal, A. Z. (2019). Murine single-cell RNA-seq reveals cell-identity- and tissue-specific trajectories of aging. *Genome Res, 29*(12), 2088-2103. doi:10.1101/gr.253880.119
- Kobayashi, H., Lei, C., Wu, Y., Mao, A., Jiang, Y., Guo, B., . . . Goda, K. (2017). Label-free detection of cellular drug responses by high-throughput bright-field imaging and machine learning. *Sci Rep*, 7(1), 12454. doi:10.1038/s41598-017-12378-4
- Kuhn, M. (2008). Building Predictive Models inRUsing thecaretPackage. *Journal of Statistical Software*, 28(5). doi:10.18637/jss.v028.i05
- LeCun, Y., Boser, B., Denker, J. S., Henderson, D., Howard, R. E., Hubbard, W., & Jackel, L. D. (1989). Backpropagation Applied to Handwritten Zip Code Recognition. *Neural Computation*, *1*(4), 541-551. doi:10.1162/neco.1989.1.4.541
- Lei, C., Kobayashi, H., Wu, Y., Li, M., Isozaki, A., Yasumoto, A., . . . Goda, K. (2018). High-throughput imaging flow cytometry by optofluidic time-stretch microscopy. *Nat Protoc*, 13(7), 1603-1631. doi:10.1038/s41596-018-0008-7
- Li, J., Barreda, D. R., Zhang, Y.-A., Boshra, H., Gelman, A. E., LaPatra, S., . . . Sunyer, J. O. (2006). B lymphocytes from early vertebrates have potent phagocytic and microbicidal abilities. *Nat Immunol*, 7(10), 1116-1124. doi:10.1038/ni1389
- Lippeveld, M., Knill, C., Ladlow, E., Fuller, A., Michaelis, L. J., Saeys, Y., . . . Peralta, D. (2020). Classification of Human White Blood Cells Using Machine Learning for Stain-Free Imaging Flow Cytometry. *Cytometry A, 97*(3), 308-319. doi:10.1002/cyto.a.23920
- Lugo-Villarino, G., Balla, K. M., Stachura, D. L., Banuelos, K., Werneck, M. B. F., & Traver, D. (2010). Identification of dendritic antigen-presenting cells in the zebrafish. *Proceedings*

857 of the National Academy of Sciences, 107(36), 15850-15855. 858 doi:10.1073/pnas.1000494107

- 859 Maizels, R. M., & Nussey, D. H. (2013). Into the wild: digging at immunology's evolutionary roots. *Nat Immunol, 14*(9), 879-883. doi:10.1038/ni.2643
 - Nassar, M., Doan, M., Filby, A., Wolkenhauer, O., Fogg, D. K., Piasecka, J., . . . Hennig, H. (2019). Label-Free Identification of White Blood Cells Using Machine Learning. *Cytometry A*, *95*(8), 836-842. doi:10.1002/cyto.a.23794
 - Nitta, N., Sugimura, T., Isozaki, A., Mikami, H., Hiraki, K., Sakuma, S., . . . Goda, K. (2018). Intelligent Image-Activated Cell Sorting. *Cell*, 175(1), 266-276 e213. doi:10.1016/j.cell.2018.08.028
 - Page, D. M., Wittamer, V., Bertrand, J. Y., Lewis, K. L., Pratt, D. N., Delgado, N., . . . Traver, D. (2013). An evolutionarily conserved program of B-cell development and activation in zebrafish. *Blood*, *122*(8), 1-12. doi:10.1182/blood-2012-12-471029
 - Palić, D., Andreasen, C. B., Ostojić, J., Tell, R. M., & Roth, J. A. (2007). Zebrafish (Danio rerio) whole kidney assays to measure neutrophil extracellular trap release and degranulation of primary granules. *J Immunol Methods*, *319*(1-2), 87-97. doi:10.1016/j.jim.2006.11.003
 - Pepe-Mooney, B. J., Dill, M. T., Alemany, A., Ordovas-Montanes, J., Matsushita, Y., Rao, A., . . . Camargo, F. D. (2019). Single-Cell Analysis of the Liver Epithelium Reveals Dynamic Heterogeneity and an Essential Role for YAP in Homeostasis and Regeneration. *Cell Stem Cell*, 25(1), 23-38 e28. doi:10.1016/j.stem.2019.04.004
 - Peuß, R., Box, A. C., Chen, S., Wang, Y., Tsuchiya, D., Persons, J. L., . . . Rohner, N. (2020). Adaptation to low parasite abundance affects immune investment and immunopathological responses of cavefish. *Nat Ecol Evol*. doi:10.1038/s41559-020-1234-2
 - Philippeos, C., Telerman, S. B., Oules, B., Pisco, A. O., Shaw, T. J., Elgueta, R., . . . Watt, F. M. (2018). Spatial and Single-Cell Transcriptional Profiling Identifies Functionally Distinct Human Dermal Fibroblast Subpopulations. *J Invest Dermatol*, 138(4), 811-825. doi:10.1016/j.jid.2018.01.016
 - R Core Team. (2014). R: A language and environment for statistical computing: R Foundation for Statistical Computing, Vienna, Austria. Retrieved from http://www.R-project.org/.
 - Rabinovitch, M. (1995). Professional and non-professional phagocytes: an introduction. *Trends in Cell Biology*, *5*(3), 85-87. doi:10.1016/s0962-8924(00)88955-2
 - Robinson, M. D., McCarthy, D. J., & Smyth, G. K. (2010). edgeR: a Bioconductor package for differential expression analysis of digital gene expression data. *Bioinformatics*, 26(1), 139-140. doi:10.1093/bioinformatics/btp616
 - Samusik, N., Good, Z., Spitzer, M. H., Davis, K. L., & Nolan, G. P. (2016). Automated mapping of phenotype space with single-cell data. *Nat Methods*, *13*(6), 493-496. doi:10.1038/nmeth.3863
 - Suzuki, Y., Kobayashi, K., Wakisaka, Y., Deng, D., Tanaka, S., Huang, C. J., . . . Ozeki, Y. (2019). Label-free chemical imaging flow cytometry by high-speed multicolor stimulated Raman scattering. *Proc Natl Acad Sci U S A, 116*(32), 15842-15848. doi:10.1073/pnas.1902322116
 - Tirosh, I., Izar, B., Prakadan, S. M., Wadsworth, M. H., 2nd, Treacy, D., Trombetta, J. J., . . . Garraway, L. A. (2016). Dissecting the multicellular ecosystem of metastatic melanoma by single-cell RNA-seq. *Science*, *352*(6282), 189-196. doi:10.1126/science.aad0501
- 702 Traver, D., Paw, B. H., Poss, K. D., Penberthy, W. T., Lin, S., & Zon, L. I. (2003). Transplantation and in vivo imaging of multilineage engraftment in zebrafish bloodless mutants. *Nat Immunol, 4*(12), 1238-1246. doi:10.1038/ni1007

- Traver, D., Paw, B. H., Poss, K. D., Penberthy, W. T., Lin, S., & Zon, L. I. (2003). 905 906 Transplantation and in vivo imaging of multilineage engraftment in zebrafish bloodless 907 mutants. Nat Immunol, 4(12), 1238-1246. doi:10.1038/ni1007
- 908 van der Meer, W., Scott, C. S., & de Keijzer, M. H. (2004). Automated flagging influences the 909 inconsistency and bias of band cell and atypical lymphocyte morphological differentials. 910 Clin Chem Lab Med, 42(4), 371-377. doi:10.1515/CCLM.2004.066

911

912

913

914

915

916

924

925

926

931

- Walt, S. v. d., Colbert, S. C., & Varoquaux, G. (2011). The NumPy Array: A Structure for Efficient Numerical Computation. Computing in Science & Engineering, 13(2), 22-30. doi:10.1109/MCSE.2011.37
- Walters, D. R. (1970). Hemocytes of saturniid silkworms: Their behaviorin vivo andin vitro in response to diapause, development, and injury. Journal of Experimental Zoology, 174(4), 441-450. doi:10.1002/jez.1401740407
- 917 Weber, L. M., & Robinson, M. D. (2016). Comparison of clustering methods for high-918 dimensional single-cell flow and mass cytometry data. Cytometry A. 89(12), 1084-1096. 919 doi:10.1002/cvto.a.23030
- 920 Wickham, H. (2010). stringr: modern, consistent string processing. R Journal, 2(2), 38-40.
- 921 Wickham, H. (2016). ggplot2: Elegant Graphics for Data Analysis. : Springer-Verlag New York.
- 922 Wilke, C. O. (2018). ggridges, Ridgeline Plots in 'ggplot2' (Version 0.5.1). Retrieved from 923 https://github.com/clauswilke/ggridges
 - Wittamer, V., Bertrand, J. Y., Gutschow, P. W., & Traver, D. (2011). Characterization of the mononuclear phagocyte system in zebrafish. Blood, 117(26), doi:10.1182/blood-2010-11-321448
- 927 Yakimov, B. P., Gogoleva, M. A., Semenov, A. N., Rodionov, S. A., Novoselova, M. V., Gayer, 928 A. V., ... Shirshin, E. A. (2019). Label-free characterization of white blood cells using 929 fluorescence lifetime imaging and flow-cytometry: molecular heterogeneity and 930 erythrophagocytosis [Invited]. Biomed Opt Express, 10(8), 4220-4236. doi:10.1364/BOE.10.004220

Main Figure Legends

Figure 1: Schematic representation of Image3C workflow, a method for cell clustering based on morphological features

- (A) A single cell suspension is prepared for image-based flow cytometric analyses. The cells can be labelled with any reagent working for the species of interest. The signal can highlight specific cell components (e.g., nuclei), metabolic cell states or specific cell functions. The samples are run on the ImageStream®X Mark II and 10,000 nucleated and focused events are saved for each sample as individual raw images.
- (B) IDEAS software (Amnis Millipore) is used to open the raw images, compensate for correcting fluorescent spillover, subtract background and quantify values for intrinsic morphological and fluorescent features. R (or R studio) is used to calculate the correlation between features to allow to trim the features that are redundant with others. Samples that are outliers among replicates are also removed prior the final normalization of the fluorescence intensities.
- (C) Images are clustered based on morphological and fluorescent feature values and visualized as a Force Directed Layout (FDL) graph where each dot represents one event.
- (D) R integration in FCS Express Plus software allows the visualization of cell images by clusters or specifically selected with a gate. This step allows to evaluate the morphological homogeneity of the clusters, determine if the number of clusters is appropriate and explore the phenotype/function of the cells based on visualization of individual channels.
- (E) Spearman's correlation plot of feature values by clusters is one of the options available in Image3C for plotting integrated data. This heatmap shows feature similarities and differences between cells belonging to different clusters.
- (F) If new experiments are run and new data needs to be analyzed two approaches can be taken. 1. If the goal is comparing samples belonging to the same experiment (e.g., treatment vs its control) the steps described so far from (A) to (E) can be re-applied to the new dataset including a statistical analysis to compare cluster relative abundance. This approach will produce a new set of clusters that will need to be re-annotated. Compare sets of clusters coming from multiple experiments and multiple rounds of analysis can be challenging without pre-existing knowledge of cell-type, clearly different morphologies or biomarkers that would allow to establish a unique correlation between clusters coming from different FDL graphs. 2. If the goal is integrating experiments and comparing cell type abundance between them, the use of steps (F) and (G) is suggested. A CNN classifier is trained using the images obtained from homeostasis, naïve or WT cells and already organized in clusters in an unbiased way through the first part of our method. This will generate a trained classifier with CNN classes based on FDL clusters.
- (G) This classifier is then used for deconvoluting data from new experimental sets and assigning each event to a CNN class with a given probability. This provides high-throughput, and unbiased way to compare different experiment sets without the requirement for pre-existing knowledge about the tissue cell types, cell biomarkers or the need to cross-annotate cluster increasing the probability to introduce errors.
- The entire pipeline chart and step-by-step technical information, such as software used, time required for processing and exported file format are reported in the interactive map Figure 1-figure supplement 1, that automatically direct to the specific section of the GitHub.

Figure 2: Analysis of cell composition of adult zebrafish WKM

- (A) WKM tissue obtained from zebrafish is prepared for image-based flow cytometric analyses and run on the ImageStream®X Mark II (n=8). Standard gating of focused and nucleated events and manual outgating of most erythrocytes was performed using IDEAS software (Amnis Millipore). The selected images were processed through the pipeline described in Figure 1 and clustered based only on intrinsic morphological and fluorescent feature values. FDL graph visualizes 16 clusters and each color represent a unique cell cluster.
- (B) Representative cell images belonging to each cluster are shown to evaluate the homogeneity of the cluster and determine morphology of the cells for cluster annotation. Representative cells for all the identified clusters are shown in Supplementary File 4. Merge represents the overlay of brightfield (BF), side scatter signal (SSC) and Draq5 (nuclear staining) signal.

- (C) Spearman's correlation plot shows the average feature values of the images in each cluster to highlight morphological similarities and differences between events belonging to different clusters, such as cell size or cytoplasm granularity (Supplementary File 1).
- (D) Box plot of relative abundance of events within each cluster follows the same color-code used in A.

Figure 3: Identification of professional phagocytes in zebrafish WKM

- (A) A phagocytosis assay was performed on a cell suspension obtained from zebrafish WKM tissue and the samples were subsequently run on the ImageStream®X Mark II (n=6). FDL graph shows 26 clusters and each color represents a unique cell cluster. Representative cell images belonging to the 4 clusters containing professional phagocytes are shown. Representative cells for all the identified clusters are shown in Supplementary File 7. Merge represents the overlay of DHR (ROS indicator), CTV (*S. aureus* labeling) and Draq5 (nuclear staining) channels. Supplementary File 2 reports the features used for this clustering.
- (B) Volcano Plot illustrates comparison of cluster relative abundance between phagocytosis samples (CTV-S. aureus) and inhibited-phagocytosis samples (CTV-S. aureus + CCB). The log fold change (logFC) is plotted in relation to the FDR (Fold Discovery Rate) corrected p-value (-log₁₀) of each individual cluster calculated with negative binomial regression model (n=6) (Supplementary File 5). Dot color follows the same color-code used in A.
- (C) Box plot of relative abundances of events within the 4 clusters containing professional phagocytes. Phagocytosis samples (CTV-S. aureus), CCB inhibited-phagocytosis samples (CTV-S. aureus + CCB) and ice inhibited-phagocytosis samples (CTV-S. aureus + Ice) (Figure 3-figure supplement 2). Statistically significant differences are calculated using the negative binomial regression model between the phagocytosis and the inhibited-phagocytosis samples (Supplementary File 5,6). ** indicates p \leq 0.01 and n.s. indicates not significantly different after FDR (n=6).

Figure 4: Analysis of *P. canaliculata* hemocyte population using only intrinsic morphological features of the cells

- (A) Hemocytes obtained from the apple snail *P. canaliculata* are prepared for image-based flow cytometric analyses and run on the ImageStream®X Mark II (n=5). Standard gating of focused and nucleated events was performed using IDEAS software (Amnis Millipore). The selected images were processed through the pipeline described in Figure 1 and clustered based only on intrinsic morphological and fluorescent feature values. FDL graph is used to visualize the 9 identified clusters and each color represent a unique cell cluster. Representative cell images belonging to each cluster are shown to evaluate the homogeneity of the cluster and determine morphology of the cells for cluster annotation. Additional representative cells for all the identified clusters are shown in Supplementary File 8. Merge represents the overlay of brightfield (BF), side scatter signal (SSC) and Draq5 (nuclear staining) signal.
- (B) Spearman's correlation plot shows the average feature values of the images in each cluster to highlight morphological similarities and differences between events belonging to different clusters, such as cell size or cytoplasm granularity (Supplementary File 1). Cluster *Pc*6 is the one among large hemocytes with higher values in features describing cytoplasm granularity (*i.e.*, area granularity #2, intensity granularity #18 and signal granularity #11).
- 1029 (C) Box plot of relative abundance of events within each cluster following the same color-code used in A. Clusters *Pc*5 and *Pc*8, constituted by duplets and dead cells, are those with the lowest number of events, validating the protocol used to prepare these samples.

Figure 5: Identification of professional phagocytes among P. canaliculata hemocytes

- (A) A phagocytosis assay was performed on a cell suspension obtained from apple snail *P. canaliculata* hemolymph and the samples were subsequently run on the ImageStream®X Mark II (n=5). FDL graph shows 20 clusters and each color represents a unique cell cluster. Representative cell images belonging to the 2 clusters containing professional phagocytes are shown. Representative cells for all the identified clusters are shown in Supplementary File 11. Merge represents the overlay of DHR (ROS indicator), CTV (*S. aureus* labeling) and Draq5 (nuclear staining) channels. Supplementary File 2 reports the features used for this clustering.
- (B) Volcano Plot illustrates comparison of cluster relative abundance between phagocytosis samples (CTV-S. aureus) and inhibited-phagocytosis samples (CTV-S. aureus + EDTA). The log fold change

- 1043 (logFC) is plotted in relation to the FDR (Fold Discovery Rate) corrected p-value (-log₁₀) of each individual cluster calculated with negative binomial regression model (n=4) (Supplementary File 9). Dot color follows the same color-code used in A.
- 1046 (C) Box plot of relative abundances of events within the 2 clusters containing professional phagocytes. 1047 Phagocytosis samples (CTV-S. aureus), EDTA inhibited-phagocytosis samples (CTV-S. aureus + EDTA) and ice inhibited-phagocytosis samples (CTV-S. aureus + Ice) (Figure 5-figure supplement 2). Statistically significant differences are calculated using the negative binomial regression model between the phagocytosis and the inhibited-phagocytosis samples (Supplementary File 9,10). ** indicates p \leq 0.01 and n.s. indicates not significantly different after FDR (n=4).

Figure 6: Classifier training and use of Convolutional Neural Network for integrating multiple experiments

1053

1054

1055

1056

1057

1058

1059

1060

1061

1062

1063

1073

1074

1075

1076

- (A) The convolutional neural network (CNN) portion of Image3C allows the integration of multiple experiments and the analysis of additional samples assigning new events to already defined and annotated clusters without manual and potentially biased matching of clusters by the user. Images of cells obtained from homeostasis, naïve or WT samples and already clustered *de novo* in an unbiased way by Image3C are exported as TIFF files together with their cluster IDs. *P. canaliculata* hemocytes in homeostasis condition obtained from female apple snails (35,000 images) is the dataset used for training the CNN classifier. Before the training, clusters with cells with strongly overlapping morphology were merged (*Pc*1 was merged with *Pc*9 and named *Pc*1_CT; *Pc*5 was merged with *Pc*8 and named *Pc*5_CT). CT stands for Classifier Training.
- 1064 (B) The training was performed on 80% of the exported images and the testing during the training was performed on 10% of the exported images. Relative accuracy was recorded every 100 iterations for 25,000 iterations total.
- 1067 (C) The training was performed on 80% of the exported images and the testing during the training was performed on 10% of the exported images. Loss calculation was recorded every 100 iterations for 25,000 iterations total and indicates that the training set is not memorized.
- 1070 (D) The True match probability (probability that trained classifier-assigned cluster matches original cluster 1071 ID) is given for each cell of the remaining 10% of the original exported images. The detailed precision 1072 score for each cluster together with the weighted average (correcting for support) is reported in the table.
 - (E) The CNN classifier allows for integrating experiments, such as phagocytosis assay and morphological assay, with minimal probability of introducing errors because of lack of biomarkers. The plot shows the distribution of the cells belonging to the snail professional phagocytes clusters (*Pc5_P* and *Pc17_P* from Figure 5, phagocytosis assay) among the clusters defined by morphological features using homeostasis conditions.
- 1078 (F) The CNN classifier allows also for the analysis of new samples obtained from the same species and 1079 the same tissue used for the training. The new events obtained running male P. canaliculata hemocytes, 1080 are assigned to clusters defined by the de novo clustering step, allowing for comparison between 1081 samples (females vs males) and statistical analysis for cluster relative abundance differences. The box 1082 plot shows the comparison of the hemocyte population composition between females and males (n=5). 1083 *** are clusters with abundances robustly significantly different between female and male animals. (*) are 1084 cluster with p-value lower than 0.05, but whose abundances are no more significantly different after the 1085 correction for multiple testing (FDR).
- 1086 (G) Representative cell images for each cluster belonging to female and male hemocytes dataset allows to visually compare the cells used to train the classifier (female) with cells assigned by the classifier and coming from a new set of samples (males). Brightfield (BF), side scatter signal (SSC) and Draq5 (nuclear staining) signal are shown in individual channels.

Supplemental Figure Legends

Figure 1-figure supplement 1: Interactive map of Image3C pipeline

Once the images are collected this pipeline can be followed step-by-step. Through this interactive map, it is possible to click on the different portions of the pipeline and be automatically directed to the corresponding section of the GitHub repository (https://github.com/stowersinstitute/LIBPB-1390-lmage3C), where a detailed step-by-step description of the processing, sample scripts, workflow files and example datasets are provided. The software used are color-coded throughout the pipeline, approximation of the time needed to run the individual steps is provided in light gray. The central column and the left side represent the *de novo* clustering portion of the pipeline, while the right side (green arrows) represents the use of the CNN, being trained with the clusters defined in an unbiased way from the *de novo* clustering and able to process new samples.

Figure 2-figure supplement 1: Feature correlation for morphology assay on adult zebrafish WKM An example of feature correlation and feature trimming step is shown. The correlation between feature is calculated (a) and the redundant features are removed in order to leave only one representative feature for each group of features with high correlation (b).

Figure 2-figure supplement 2: Sample correlation for morphology assay on adult zebrafish WKM Sample correlation and outlier sample removal step performed on samples of adult zebrafish WKM. The correlation between samples is calculated and samples with clear outlier profile are removed from the subsequent analysis.

Figure 2-figure supplement 3: DNA normalization for morphology assay on adult zebrafish WKM An example of DNA normalization step is shown. The fluorescent peaks of DNA staining for all the samples of one experiment are shown before (a) and after (b) normalization that aims to align the 2N and 4N peaks across samples.

Figure 3-figure supplement 1: Sample correlation for phagocytosis assay on adult zebrafish WKM Sample correlation and outlier sample removal step performed on samples of adult zebrafish WKM after phagocytosis assay. The correlation between samples is calculated and samples with clear outlier profile are removed from the subsequent analysis.

Figure 3-figure supplement 2: Phagocytosis assay on adult zebrafish WKM (ice phagocytosis inhibition)

Volcano Plot illustrates comparison between phagocytosis samples (CTV-*S. aureus*) and inhibited-phagocytosis samples (CTV-*S. aureus* + Ice). The log fold change (logFC) is plotted in relation to the FDR (Fold Discovery Rate) corrected p-value (-log₁₀) of each individual cluster calculated with negative binomial regression model (n=6) (Supplementary File 6). Dot color follows the same color-code used in Figure 3A.

Figure 4-figure supplement 1: Sample correlation for morphology assay on *P. canaliculata hemocytes*

Sample correlation and outlier sample removal step performed on samples of *P. canaliculata* hemocytes. The correlation between samples is calculated and samples with clear outlier profile are removed from the subsequent analysis.

Figure 5-figure supplement 1: Sample correlation for phagocytosis assay on *P. canaliculata* hemocytes

Sample correlation and outlier sample removal step performed on samples of *P. canaliculata* hemocytes after phagocytosis assay. The correlation between samples is calculated and samples with clear outlier profile are removed from the subsequent analysis.

Figure 5-figure supplement 2: Phagocytosis assay on *P. canaliculata* hemocytes (ice phagocytosis inhibition)

Volcano Plot illustrates comparison between phagocytosis samples (CTV-*S. aureus*) and inhibited-phagocytosis samples (CTV-*S. aureus* + lce). The log fold change (logFC) is plotted in relation to the FDR (Fold Discovery Rate) corrected p-value (-log₁₀) of each individual cluster calculated with negative binomial regression model (n=4) (Supplementary File 10). Dot color follows the same color-code used in Figure 5A.

Figure 5-figure supplement 3: Feature heatmap after phagocytosis assay on *P. canaliculata* hemocytes

Spearman's correlation plot shows the average feature values of the images in each cluster to highlight morphological similarities and differences between events belonging to different clusters, such as cell size or cytoplasm granularity (Supplementary File 2). The clusters with higher DHR signal and high bacteria are the one identified as containing professional phagocytes (*Pc5_P* and *Pc17_P*). This is also confirmed by the statistical analysis performed between the phagocytosis samples (CTV-*S. aureus*) and inhibited-phagocytosis samples (CTV-*S. aureus* + EDTA) (Figure 5B; Supplementary File 9).

Figure 5-figure supplement 4: Gallery of P. canaliculata hemocytes after phagocytosis assay

Representative cell images side-by-side of professional phagocytes and non-phagocytic hemocytes from apple snail samples after phagocytosis assay. The signal of the bacteria labelled with cell-trace-violet is showed in yellow and the value for the signal intensity has been reported on top of each individual image. These images were obtained using the gallery function of the Amnis IDEAS software and manually gating events double positive for both DHR and bacteria and events double negative.

Main Table 1167

Table 1: Extensive overview on label-free cell clustering tools including a comparison of their main features.

Tool name	Was tested on multiple cell types?	Requires a priori knowledge of the sample and/or species-specific reagents for the clustering?	Uses commercially available hardware?	Uses free or open source softwares?
Image3C (present work)	YES (Zebrafish whole kidney marrow; Apple snail hemolymph)	NO Does not require previous knowledge or species-specific reagents to cluster cell images and train the neural network. If available, they can be used/integrated.	YES (ImageStream)	YES (IDEAS; Vortex; R; Python) NO (FCS Express Plus)
CellProfiler ^a	YES (Fixed Jurkat cells; Live Jurkat cells; Fission yeast; Human white Blood Cells)	YES Requires annotated datasets to train the machine learning algorithms, either by staining the samples with known markers, or by manually clustering the cells.	YES (ImageStream; microscope)	YES (IDEAS; CellProfiler; MATLAB)
CellProfiler Analyst ^b	NO (Jurkat cells)	YES Requires the use of fluorescent markers to annotate the cells and use them as the ground truth to train the machine-learning algorithms.	YES (ImageStream)	YES (IDEAS; CellProfiler or Phyton or MATLAB)
Label-free reflectance microscopy ^c	NO (Fixed HeLa cells)	YES Requires Immuno-Fluorescence images with known markers to use as ground truth and for training multiple deep learning models.	NO (Custom-built multimodal light-emitting diode (LED) array reflectance microscope)	YES (Deep neural networks)
Optofluidic time- stretch microscopy ^d	NO (Human breast adenocarcinoma cell line, MCF-7)	YES Does not provide cell clustering and single cell resolution analysis. The changes are analyzed overall in the sample without assigning it to a cell type.	NO (Optofluidic time-stretch microscope and microfluidic devices)	YES (MATLAB)
Raman scattering e	YES (Microalgal cells; Circulating tumor cells in human blood)	YES Requires homogenous cell cultures. After different treatments, these samples are used to create databases for training the deep learning.	NO (High-speed multicolor stimulated Raman scattering (SRS) microscope and microfluidic platform)	YES (Deep learning, neural network structure, VGG-16)

 $^{^{\}rm a}$ Blasi et al., 2016; Nassar et al., 2019

b Henning et al., 2017

c Cheng et al., 2021 d Kobayashi et al., 2017

e Suzuki et al., 2019

Fluorescence lifetime imaging f (Human White Blood Cells)	YES Dependent on other techniques to identify cell type to compare their autofluorescence signals and fluorescence decay for further analysis.	YES (Fluorescence Microscopy, FLIM and Flowcytometer)	YES (Python)
---	---	---	-----------------

^f Yakimov et al., 2019

Supplemental Data Files

1169 1170 1171

1172

1173

1175 1176

1177

1178

1179

1180 1181

1182

1183

1184

1185 1186

1187

1188

1189

1190 1191

1192

1193

1194

1195

1196 1197

1198

1199

1200

1201

1202 1203

1204

1205

1206

1207

1208 1209

1210

1211

1212

1213 1214

1215

1216

1217

1218

1219

1220 1221

1222

Supplementary File 1: Features used for the morphology assay

Names and descriptions of the features quantified by IDEAS software and used for clustering events based on cell morphology in the homeostasis cell composition experiment. BF is Bright Field, CI is Cell 1174 Intrinsic, CF is Cell Function.

Supplementary File 2: Features used for the phagocytosis assay

Names and descriptions of the features quantified by IDEAS software and used for clustering events based on cell morphology and function in the phagocytosis experiment. BF is Bright Field, CI is Cell Intrinsic. CF is Cell Function.

Supplementary File 3: Cell cluster properties

Cell cluster properties (e.g., cell numbers per cluster, cell feature used for clustering, feature values for each cluster) for zebrafish WKM morphology and phagocytosis assay and for P. canaliculata hemocyte morphology and phagocytosis assay.

Supplementary File 4: Cell Gallery for zebrafish WKM in homeostasis condition

Representative cell images belonging to each individual cluster identified by Image3C for zebrafish WKM in homeostasis condition are shown. BF is Bright Field, SSC is Side Scatter Signal and Drag5 is nuclear staining. Merge represents the overlay of BF, SSC and Drag5.

Supplementary File 5: Phagocytosis vs phagocytosis inhibited with CCB on zebrafish WKM

Results of negative binomial regression analysis comparing cluster relative abundance between phagocytosis samples (CTV-S. aureus) vs phagocytosis inhibited with CCB samples (CTV-S. aureus + CCB) in the zebrafish phagocytosis experiment, FC is Fold Change, CPM is Count Per Million, LR is Likelihood Ratio, FDR is Fold Discovery Rate. Relative graph is reported in Figure 3B.

Supplementary File 6: Phagocytosis vs phagocytosis inhibited with ice on zebrafish WKM

Results of negative binomial regression analysis comparing cluster relative abundance between phagocytosis samples (CTV-S. aureus) vs phagocytosis inhibited with ice samples (CTV-S. aureus + Ice) in the zebrafish phagocytosis experiment. FC is Fold Change, CPM is Count Per Million, LR is Likelihood Ratio, FDR is Fold Discovery Rate. Relative graph is reported in Figure 3-figure supplement 2.

Supplementary File 7: Cell Gallery for zebrafish WKM after phagocytosis assay

Representative cell images belonging to each individual cluster identified by Image3C for zebrafish WKM after phagocytosis assay are shown. BF is Bright Field, DHR is a fluorescent ROS indicator, SSC is Side Scatter Signal, Bac is CTV signal (S. aureus labeling) and Drag5 is nuclear staining. Merge represents the overlay of DHR, Bac and Draq5.

Supplementary File 8: Cell Gallery for P. canaliculata hemocytes in homeostasis condition

Representative cell images belonging to each individual cluster identified by Image3C for snail hemocytes in homeostasis condition are shown. Ch01 is Bright Field, Ch06 is SSC (Side Scatter Signal) and Ch11 is Drag5 (nuclear staining). Merge represents the overlay of Ch01, Ch06 and Ch11.

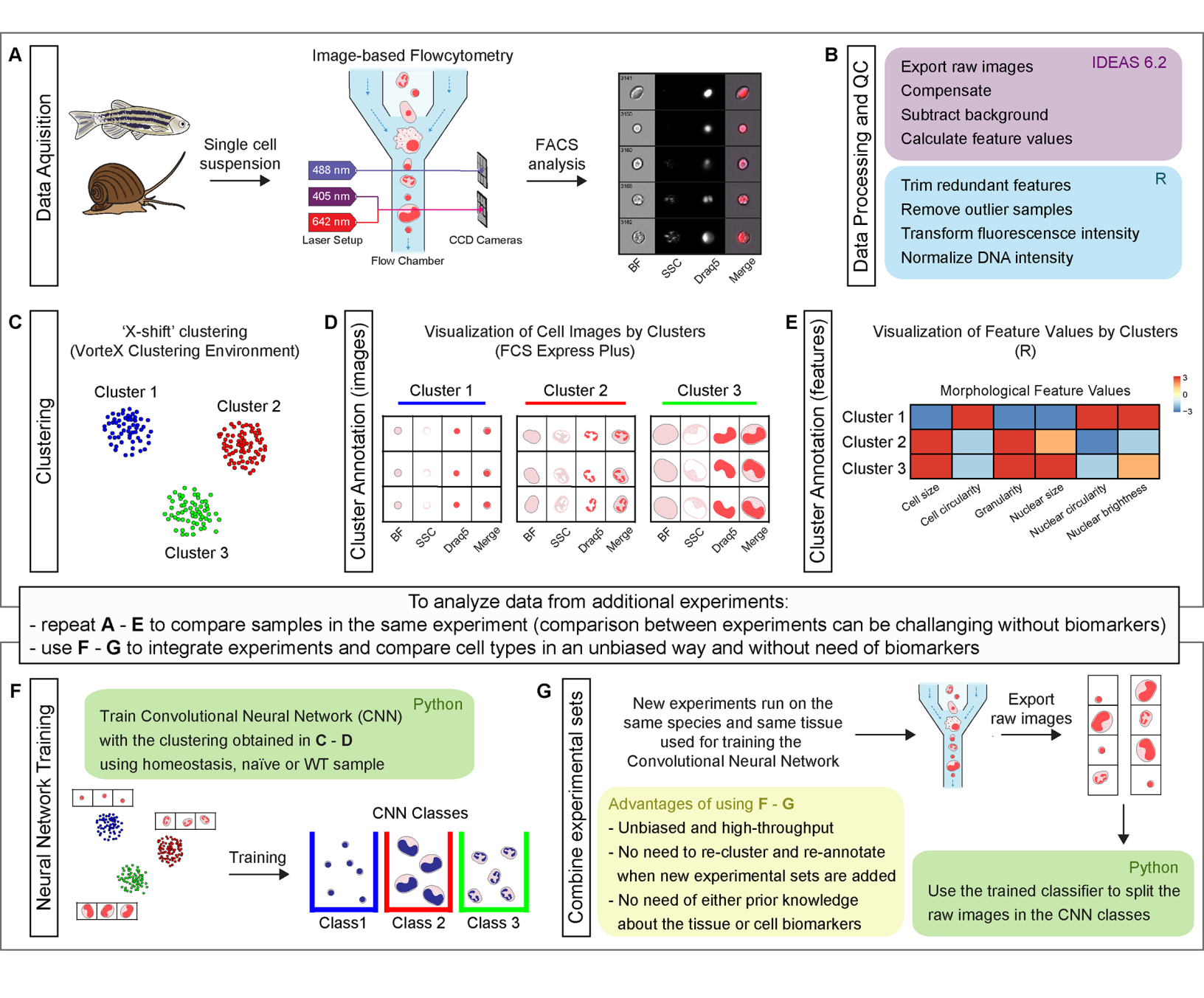
Supplementary File 9: Phagocytosis vs phagocytosis inhibited with EDTA on P. canaliculata hemocytes

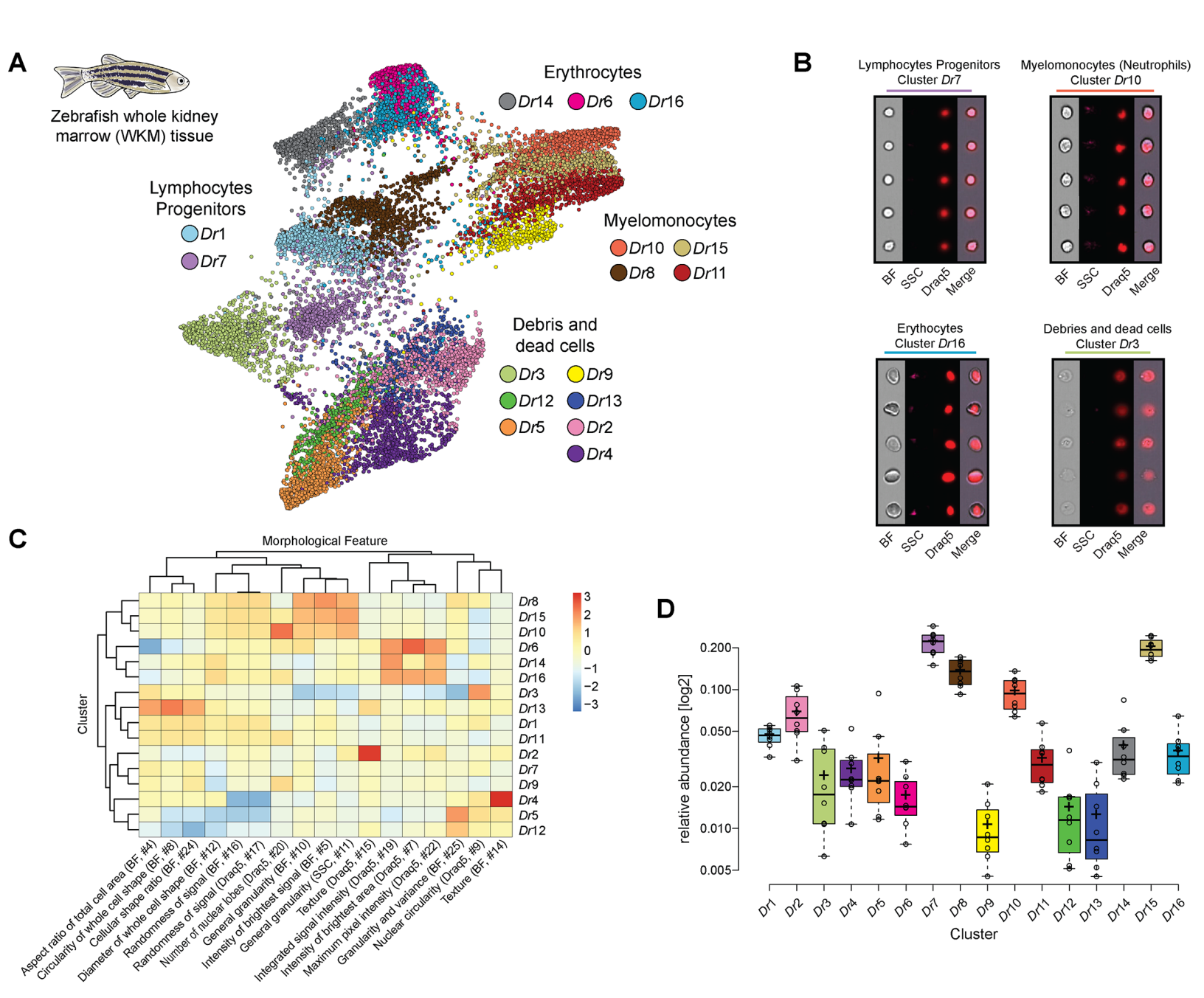
Results of negative binomial regression analysis comparing cluster relative abundance between phagocytosis samples (CTV-S. aureus) vs phagocytosis inhibited with EDTA samples (CTV-S. aureus + EDTA) in the apple snail P. canaliculata phagocytosis experiment. FC is Fold Change, CPM is Count Per Million, LR is Likelihood Ratio, FDR is Fold Discovery Rate. Relative graph is reported in Figure 5B.

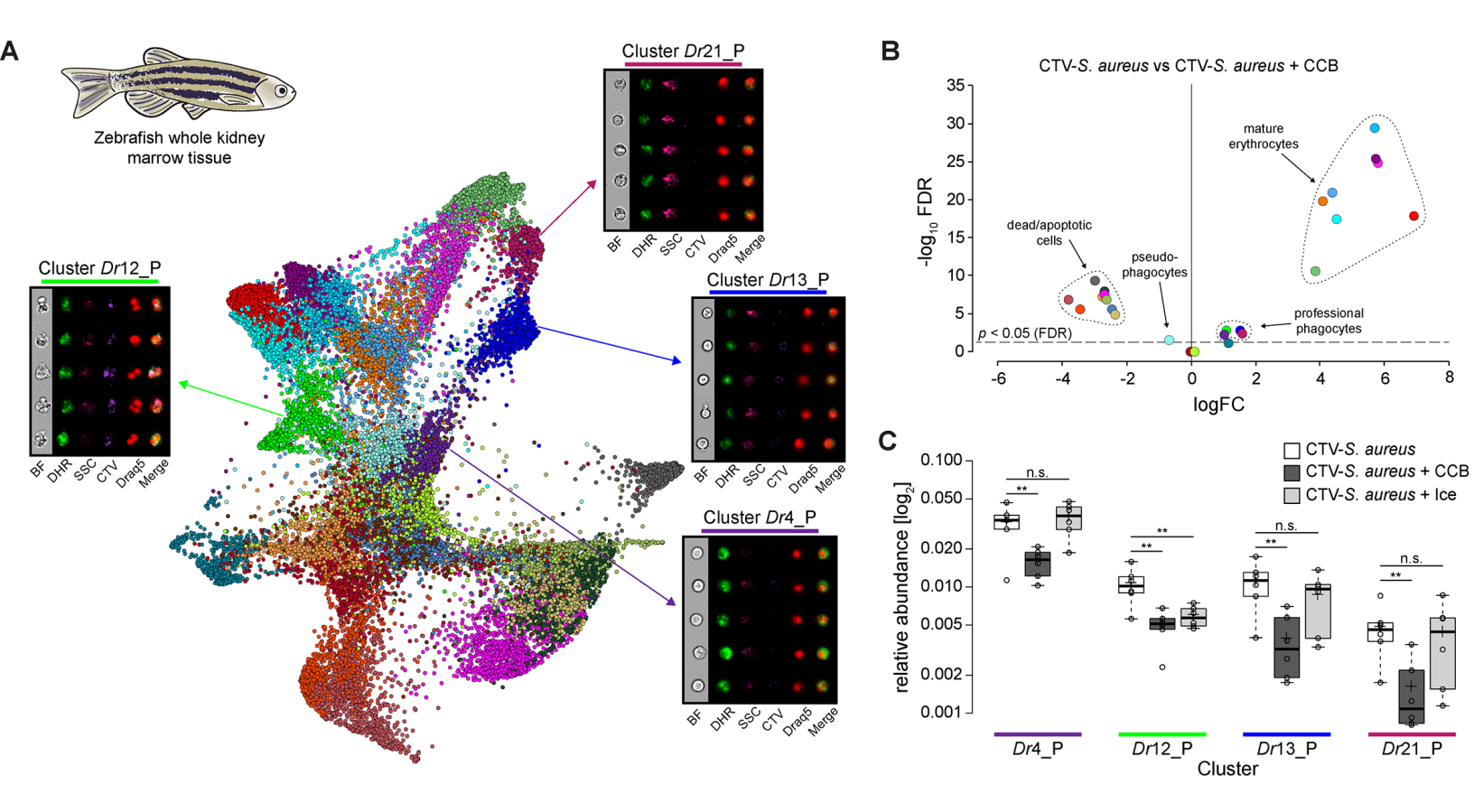
Supplementary File 10: Phagocytosis vs phagocytosis inhibited with ice on P. canaliculata hemocytes

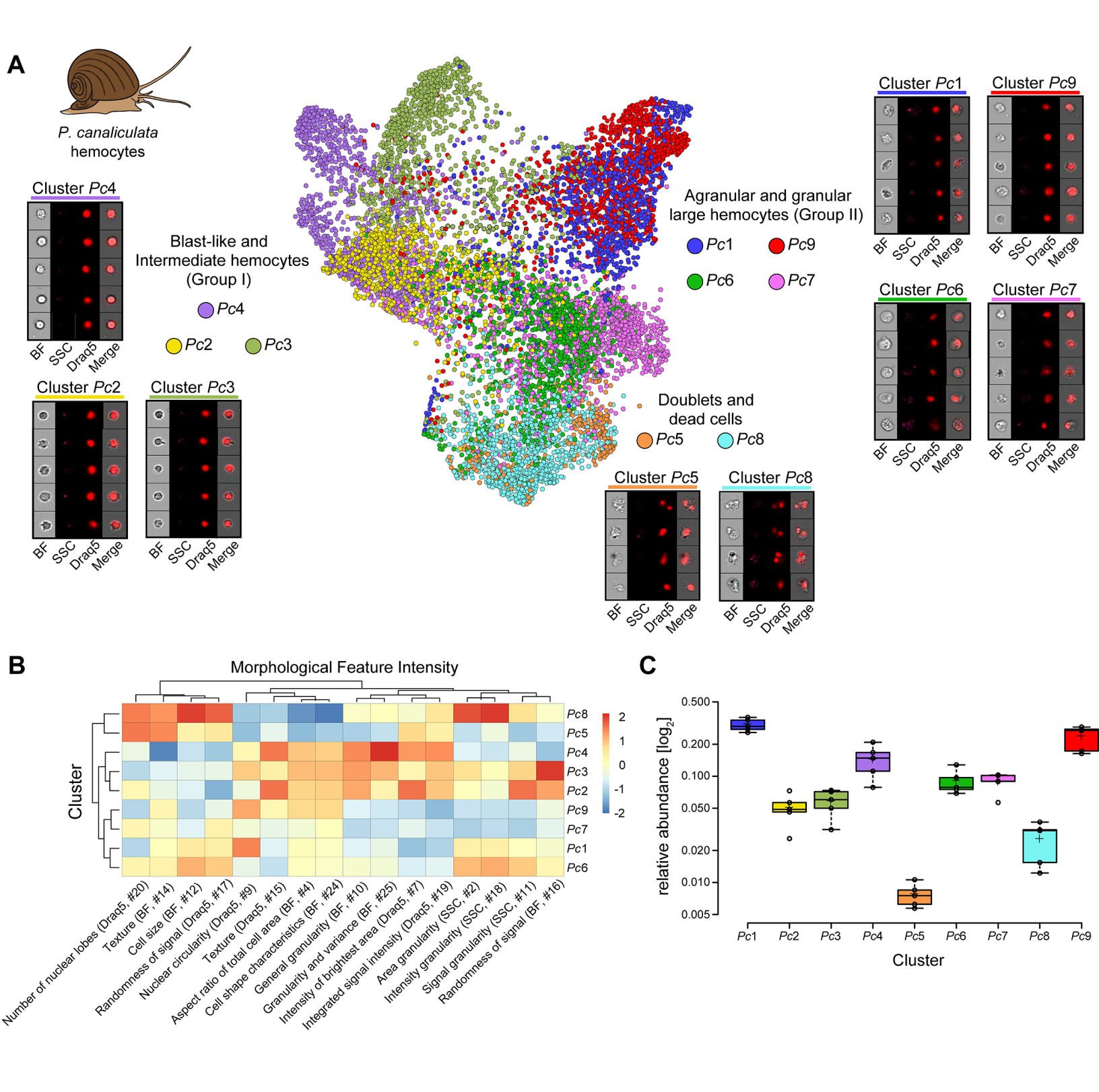
Results of negative binomial regression analysis comparing cluster relative abundance between phagocytosis samples (CTV-S. aureus) vs phagocytosis inhibited with ice samples (CTV-S. aureus + Ice) in the apple snail P. canaliculata phagocytosis experiment. FC is Fold Change, CPM is Count Per Million, LR is Likelihood Ratio, FDR is Fold Discovery Rate. Relative graph is reported in Figure 5-figure supplement 2.

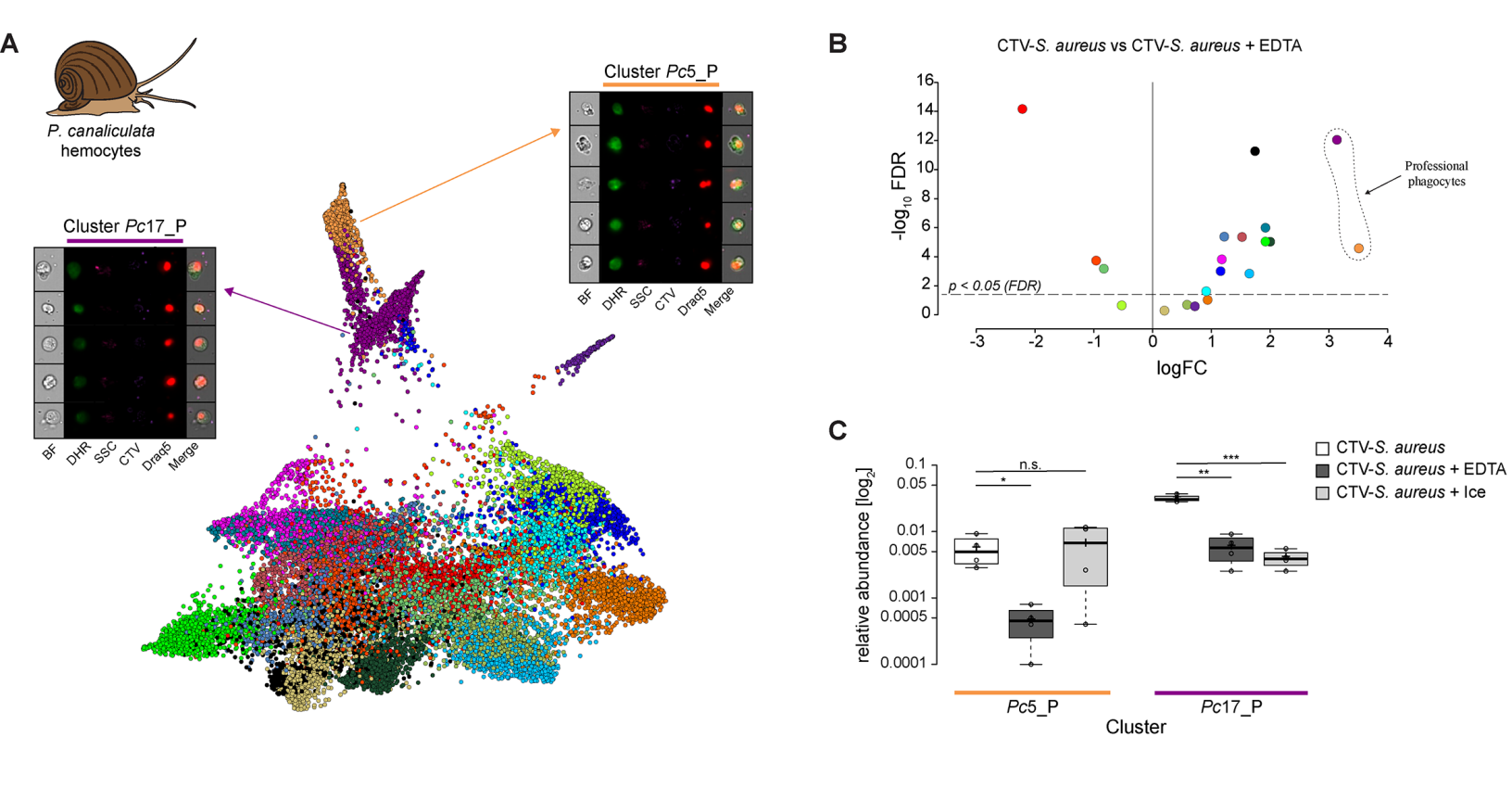
Supplementary File 11: Cell Gallery for *P. canaliculata* hemocytes after phagocytosis assay
Representative cell images belonging to each individual cluster identified by Image3C for snail hemocytes
after phagocytosis assay are shown. Ch01 is Bright Field, Ch02 is DHR signal (ROS indicator), Ch06 is
SSC (Side Scatter Signal), Ch07 is CTV signal (*S. aureus* labeling) and Ch11 is Draq5 (nuclear staining).
Merge represents the overlay of Ch02, Ch06, Ch07 and Ch11.











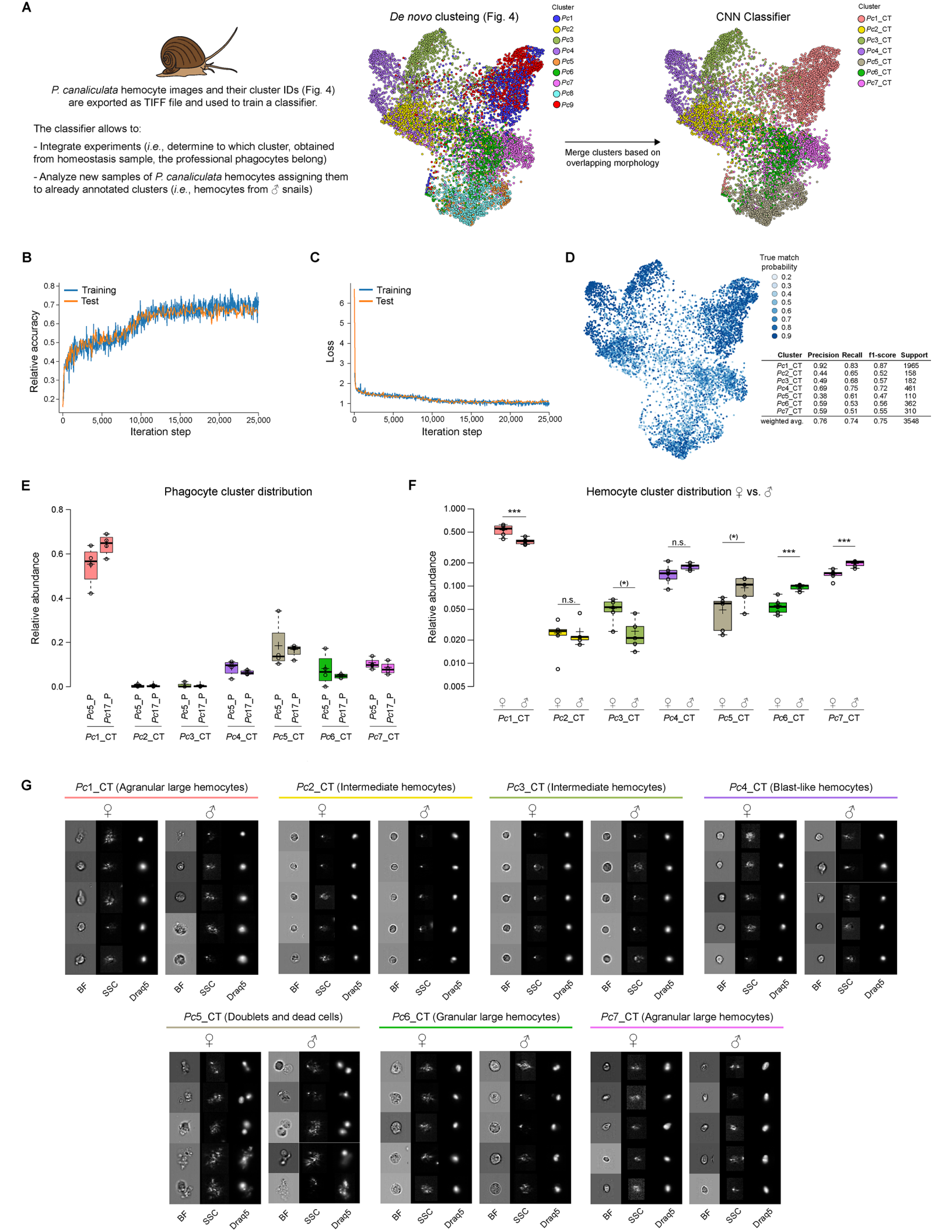
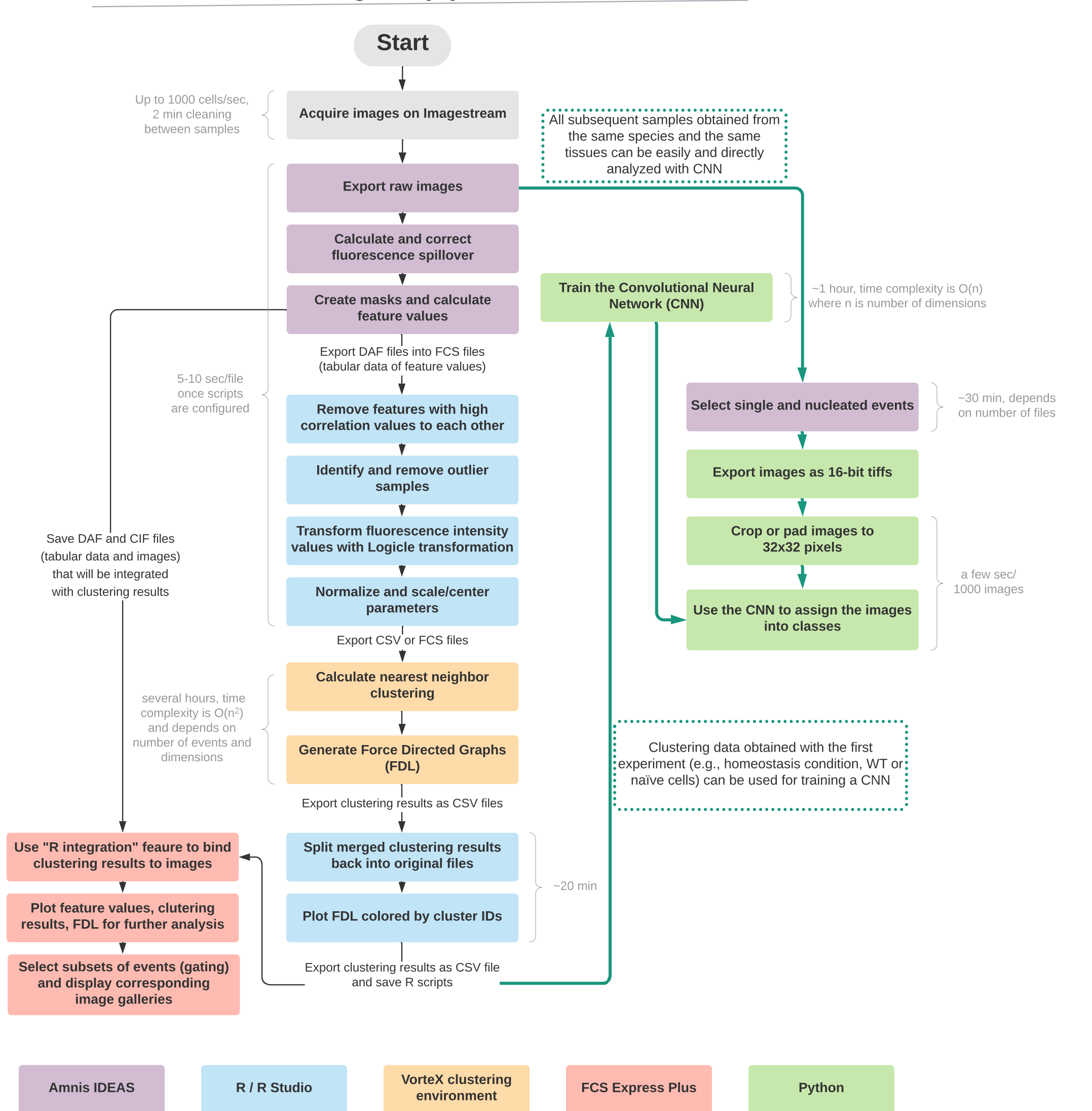
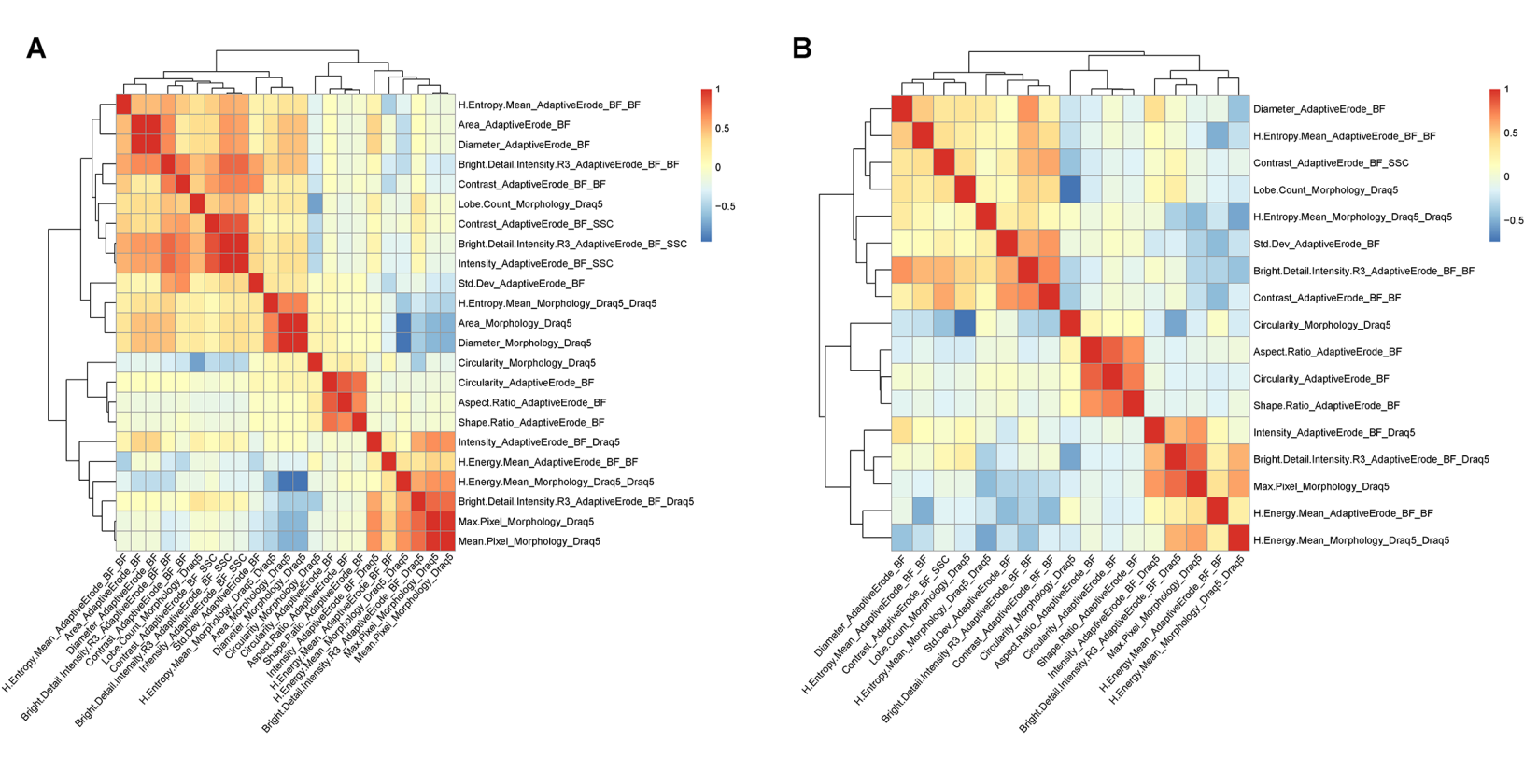
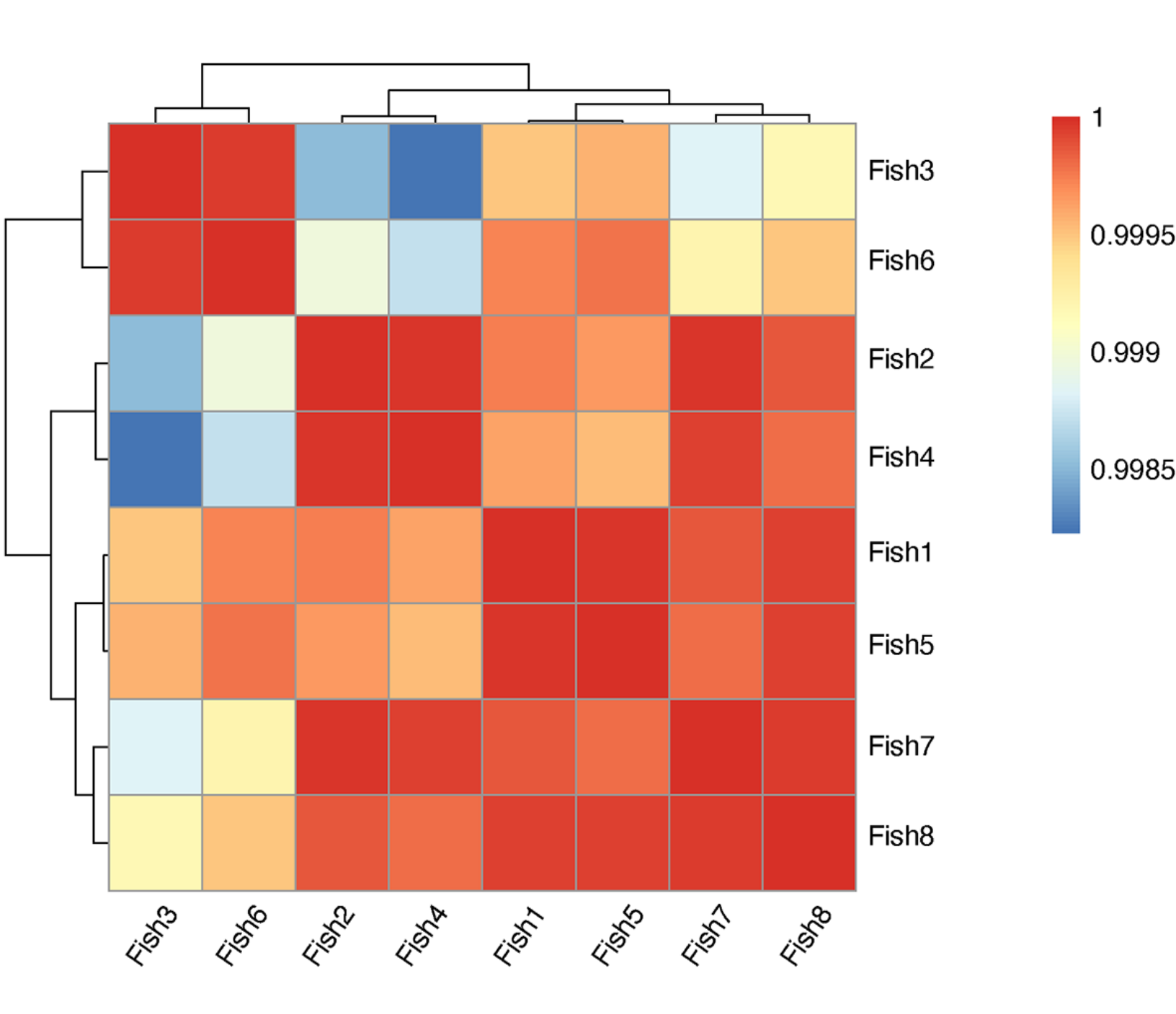
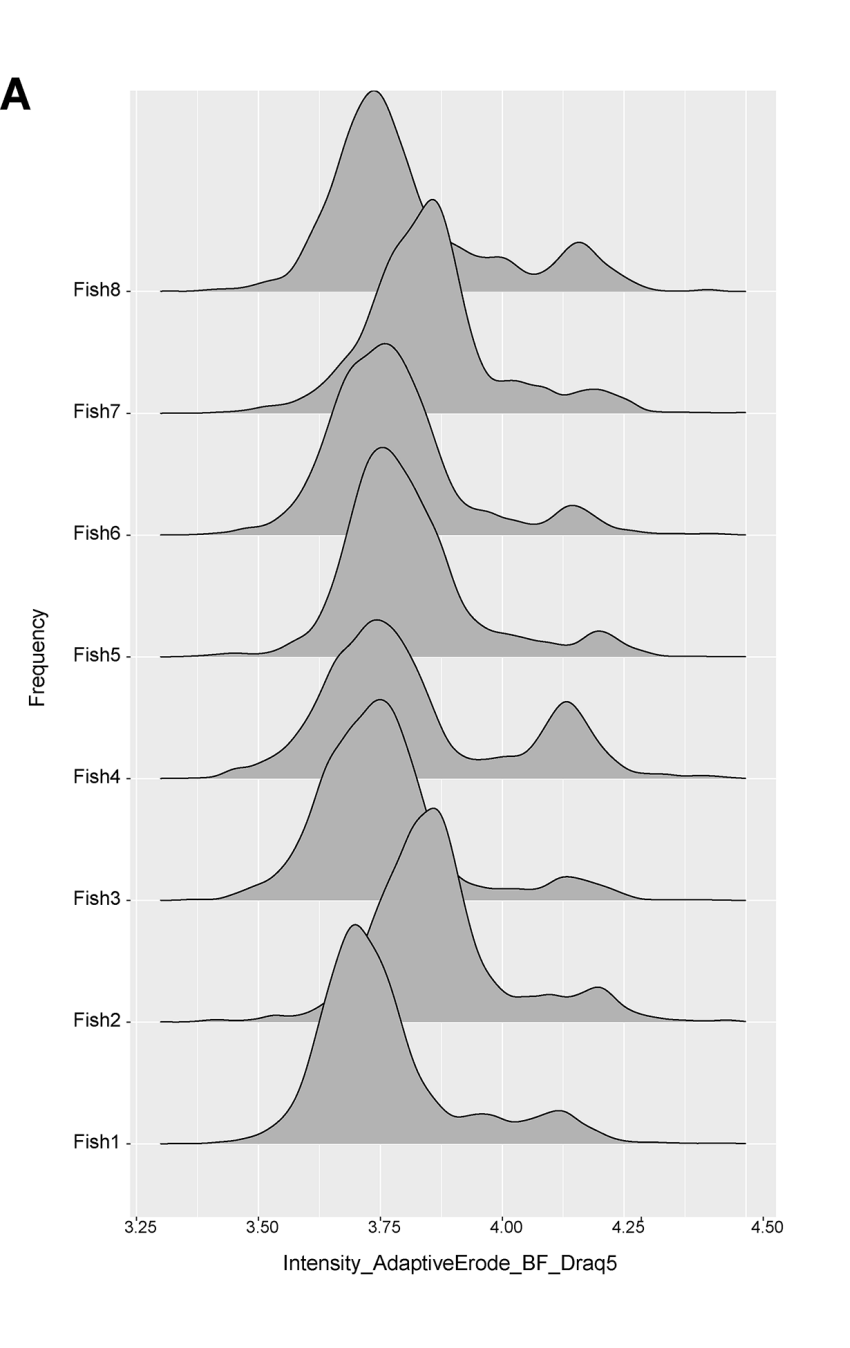


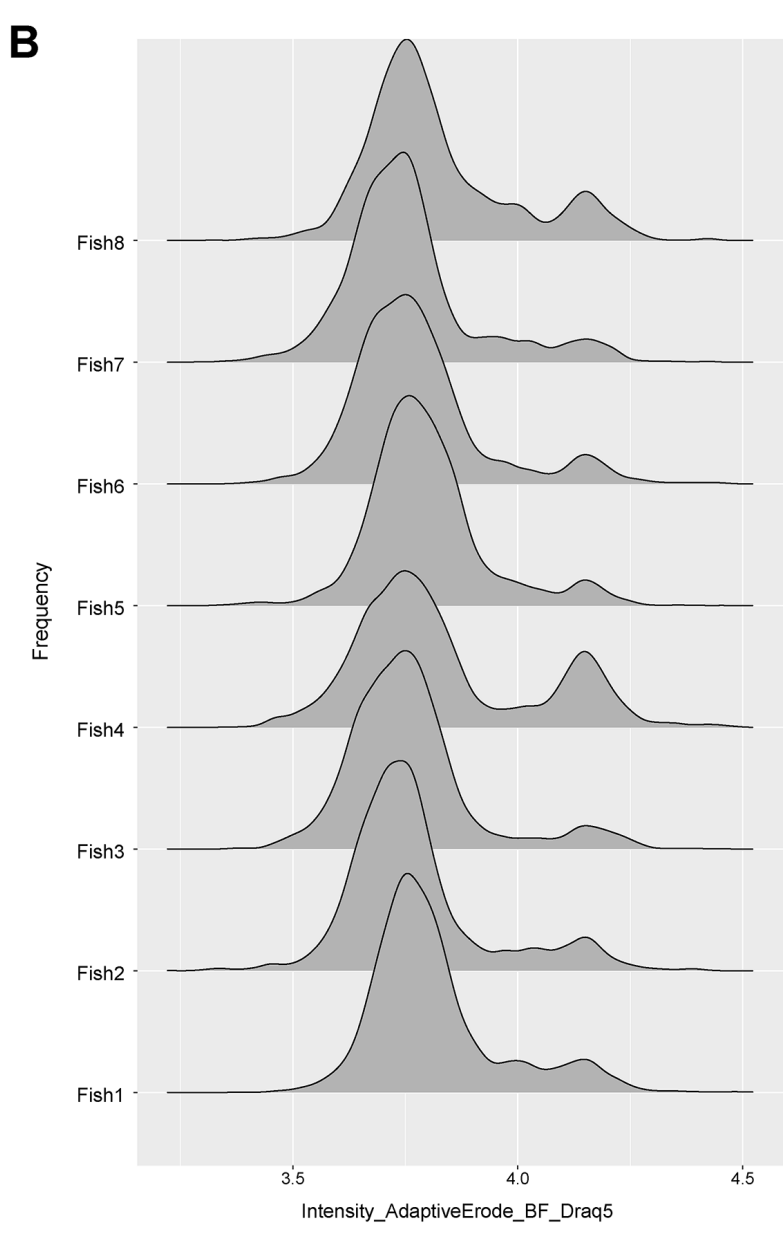
Image3C pipeline

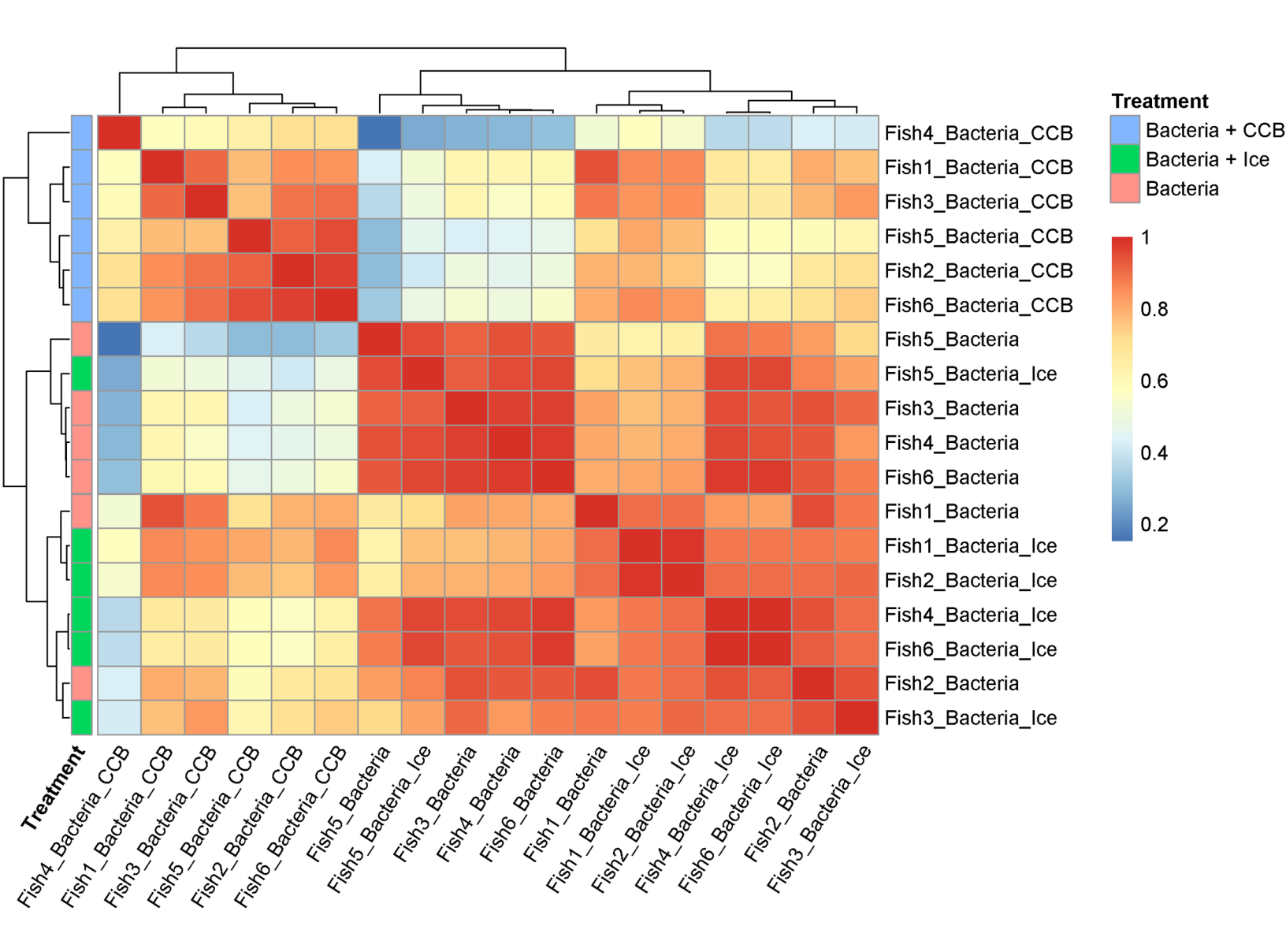




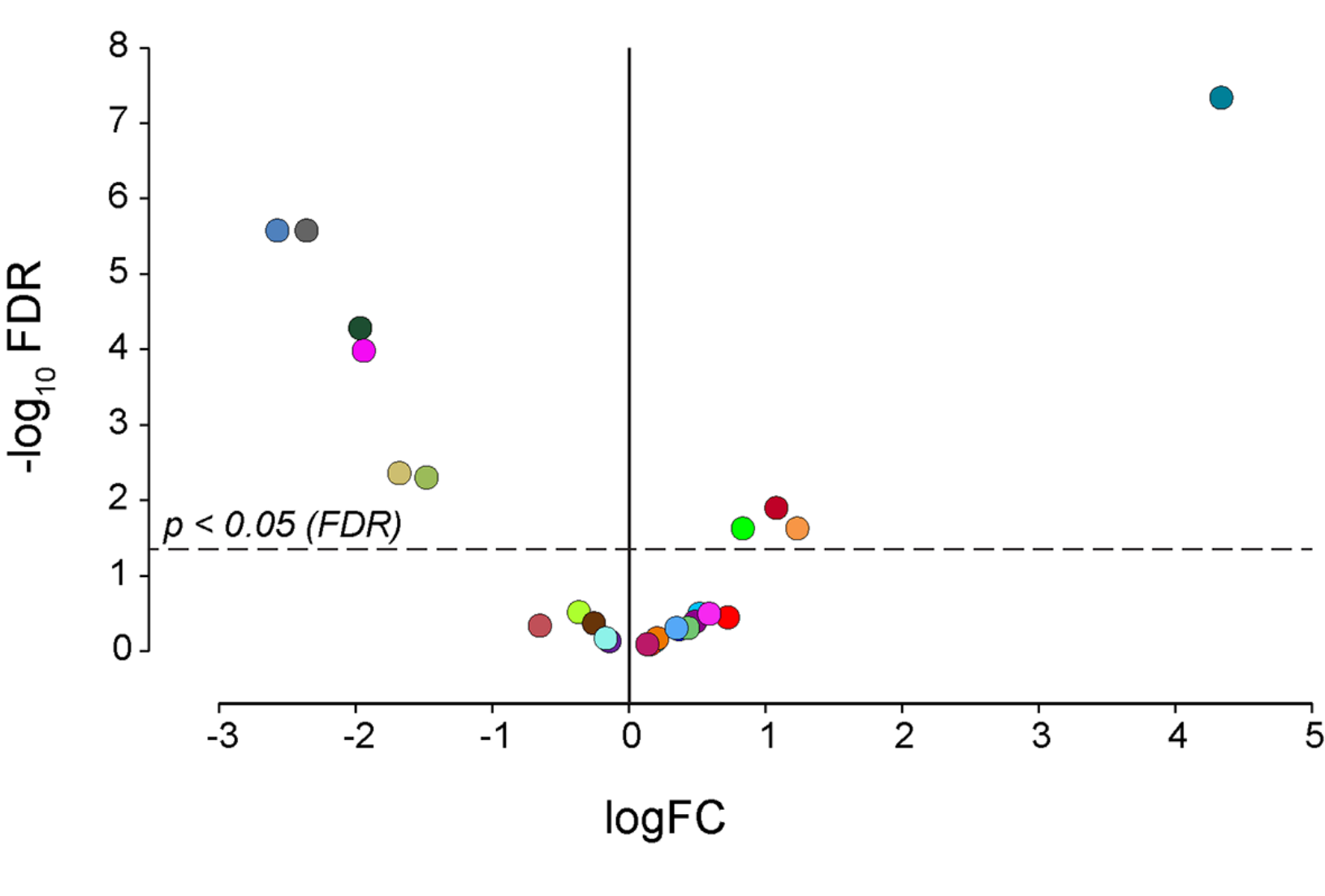


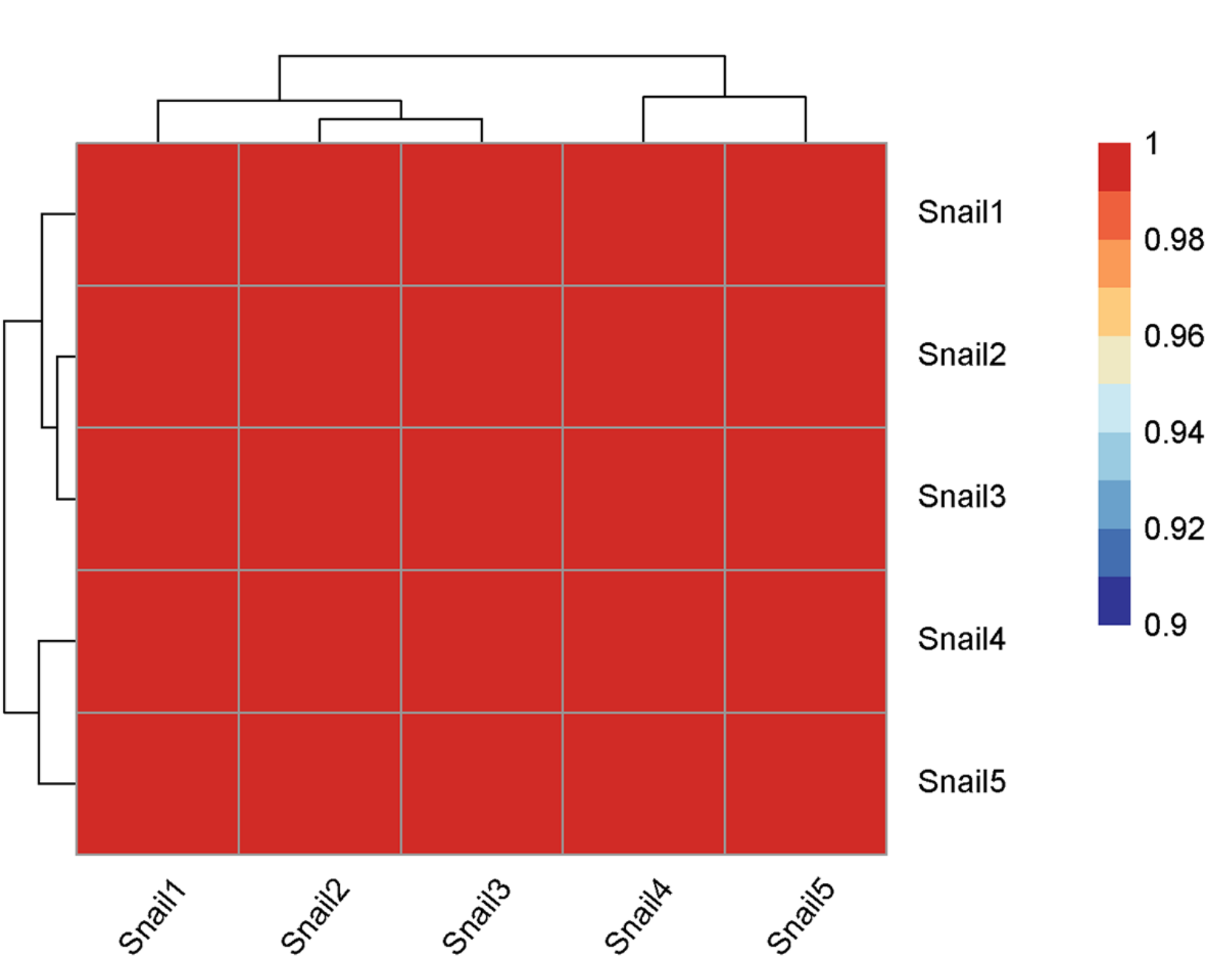


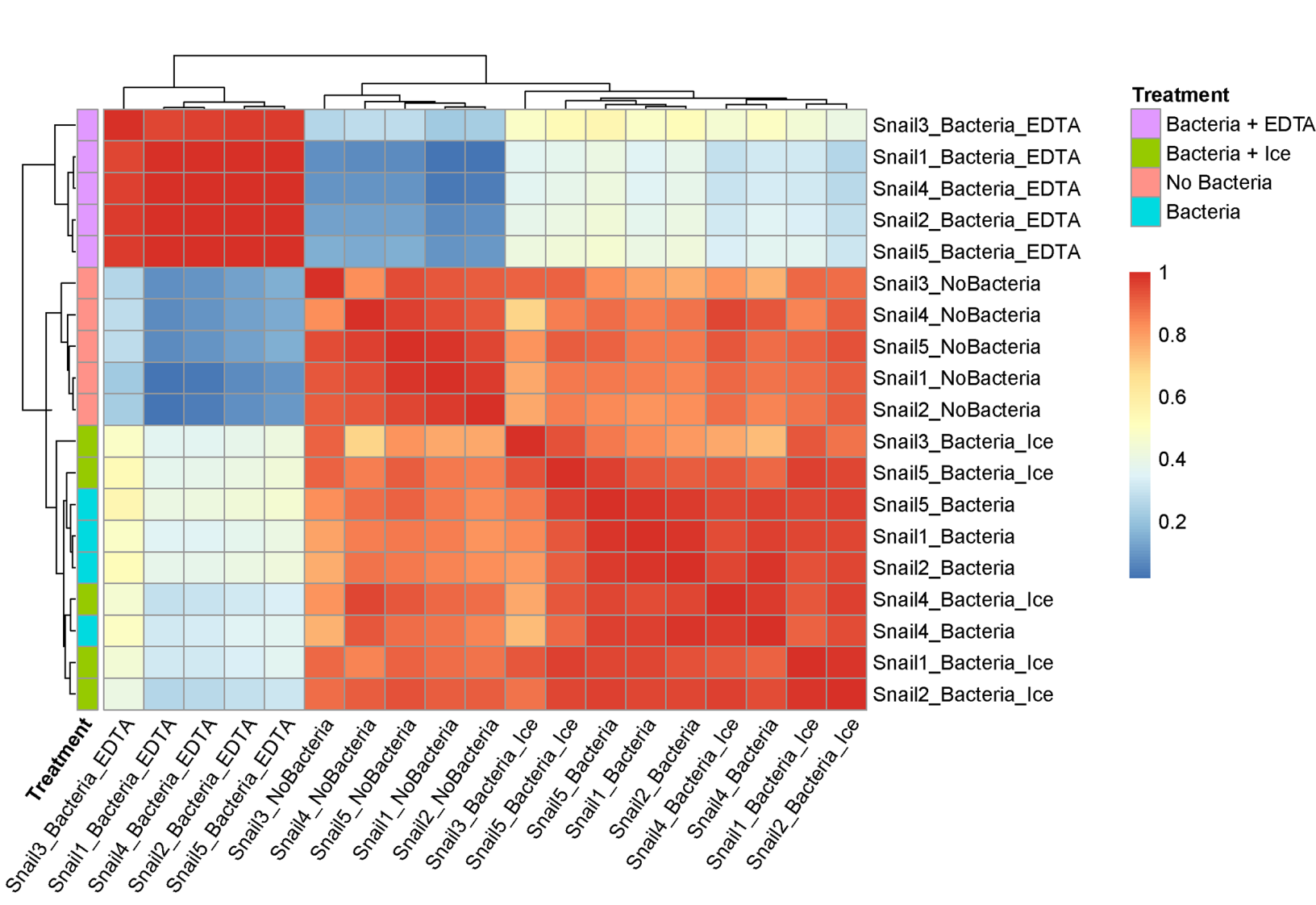




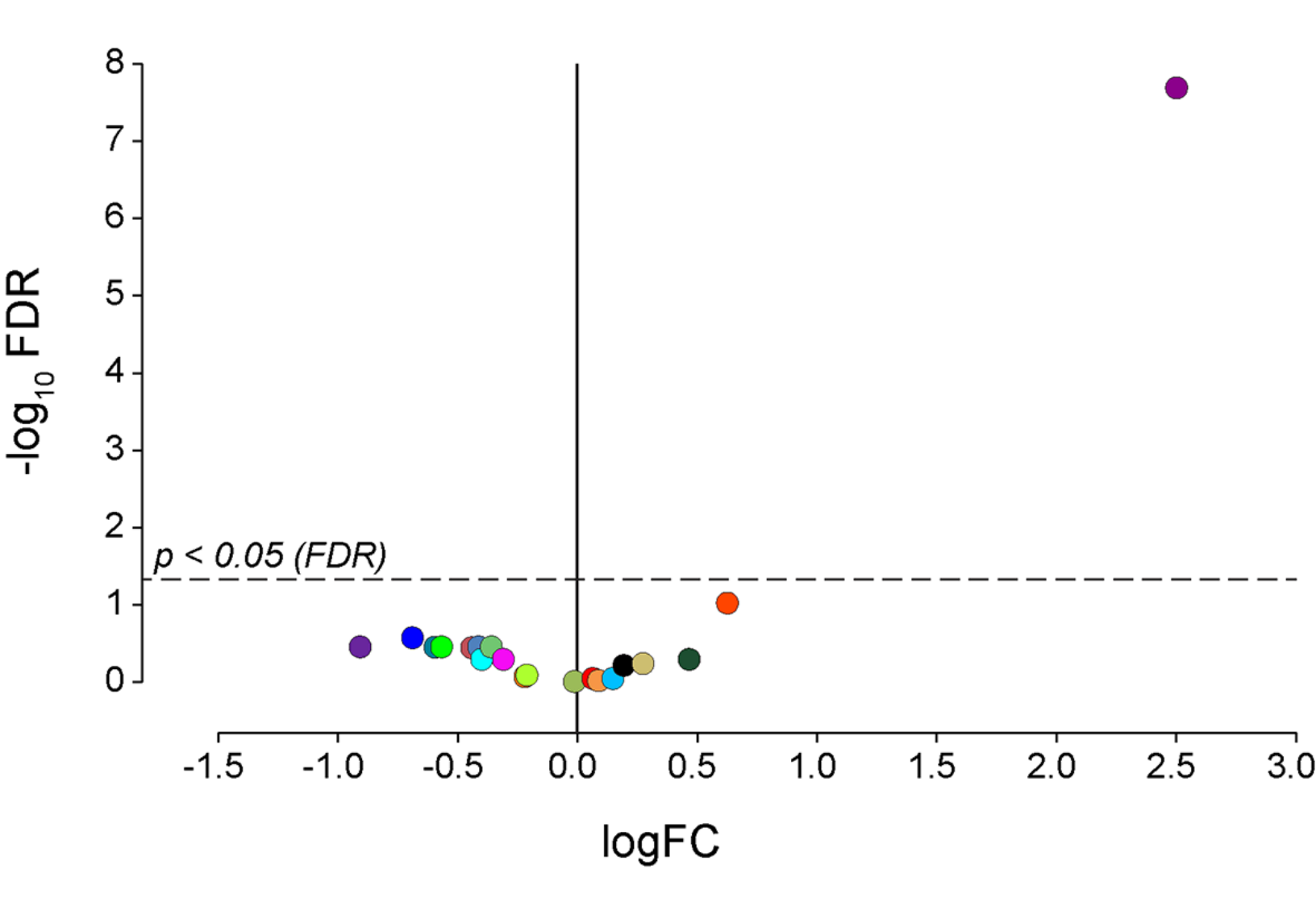
CTV-S. aureus vs CTV-S. aureus + Ice

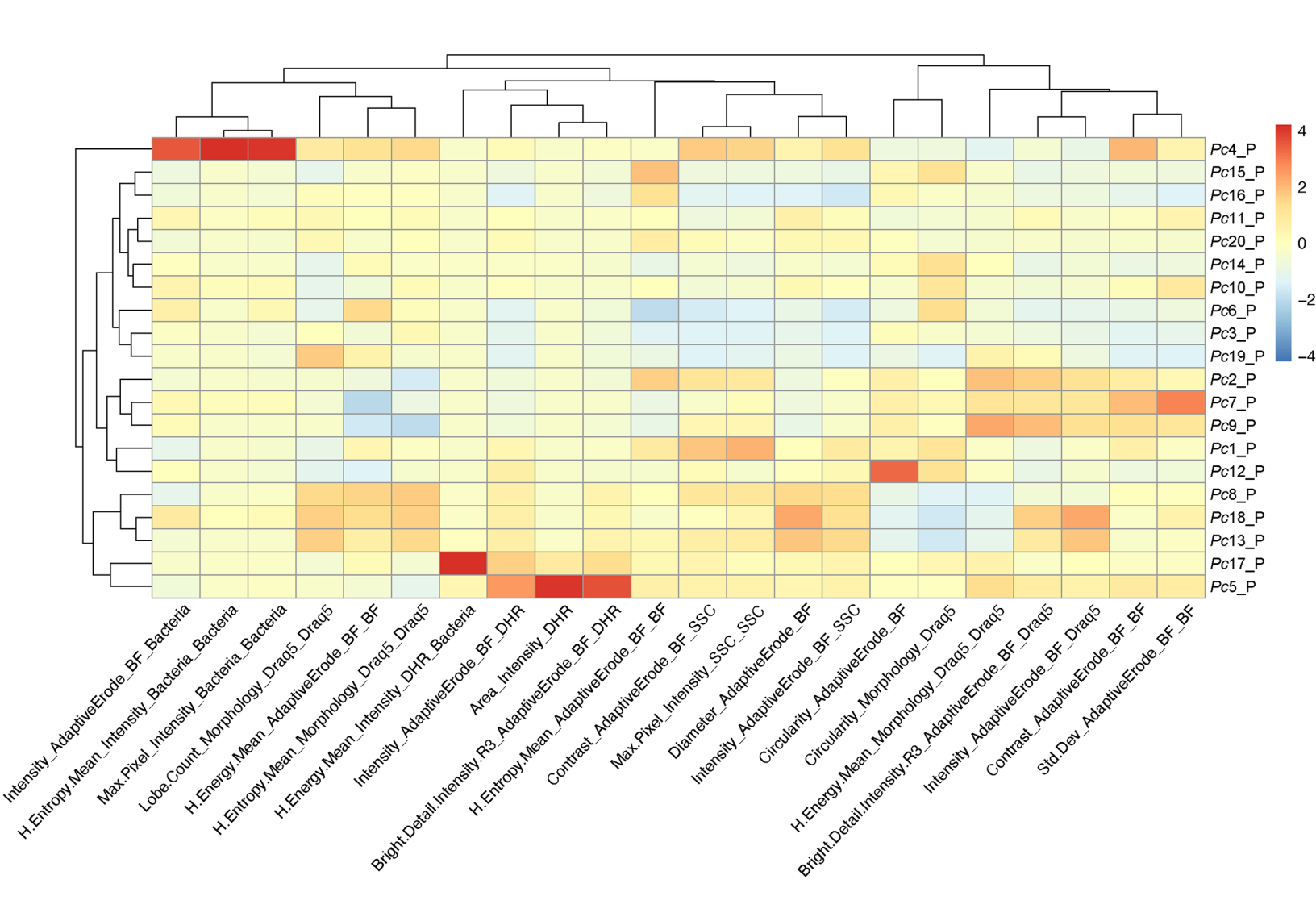


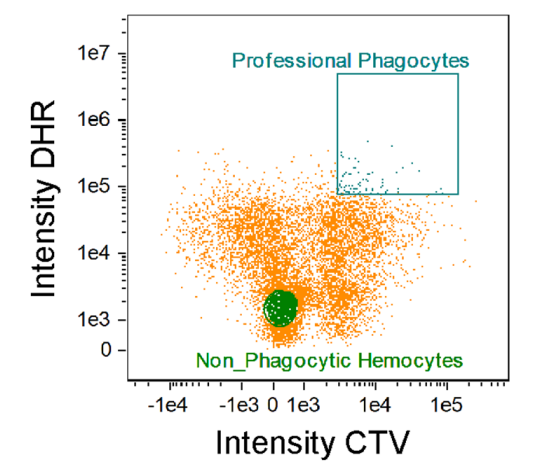




CTV-S. aureus vs CTV-S. aureus + Ice







Non-Phagocytic Hemocytes



